

# Sensitivity Analysis of Airborne Microwave Retrieval of Stratiform Precipitation to the Melting Layer Parameterization

Frank Silvio Marzano, *Member, IEEE*, and Peter Bauer

**Abstract**—A sensitivity analysis for airborne microwave passive and active retrievals of hydrometeor profiles with respect to melting-layer parameterizations is carried out using synthetic data. The parameterizations of the melting layer include the effects of snow density, particle size distributions of hydrometeors as well as different permittivity models for mixed-phase particles. The hydrometeor profiles are obtained from a two-dimensional cloud ensemble model simulating a convective-stratiform rainfall event over the East Mediterranean sea. The statistical analysis reveals that the Maxwell–Garnett mixing formulas with water matrix and ice inclusions may be chosen for graupel, while a new permittivity model from Meneghini and Liao is suitable for snowflakes. A new Bayesian inversion framework is set up for both airborne microwave radiometric, radar, and combined radar-radiometer retrievals of hydrometeor profiles. Using the cloud profiles as control training data set, a numerical analysis was carried out by testing the inversion algorithms on each melting model data set. Results are discussed in terms of estimate sensitivity, defined as the statistical deviation bounds of the retrieved profiles from the control case ones. Relatively high values of estimate sensitivity to the melting-layer parameterizations are found for all hydrometeor species, especially for low snow-density and Maxwell–Garnett dielectric model test cases. The need of including various melting-layer characterizations within a comprehensive training data set and its implications for model-based Bayesian retrieval algorithms is finally argued and numerically tested.

**Index Terms**—Microwave radiometry and radar meteorology, precipitation retrieval, radiative transfer modeling, spaceborne remote sensing.

## I. INTRODUCTION

THE contribution of stratiform rainfall to total precipitation amounts to 70% over the globe and up to 50% in the tropics [1]. It may originate from nimbostratus clouds accompanying warm fronts or from stages of decaying convective storms. It is rather uncommon to observe a pure stratiform rainfall system. Stratiform precipitation is mostly embedded in convective systems and particle melting itself may lead to

local instabilities leading to convective overturning [2]. Surface rainrates in a stratiform precipitation rarely exceed 15–20 mm/h. The main characteristics of stratiform precipitating cloud is its comparably horizontal spatial homogeneity, with a vertical cloud extent generally below 7–8 km, and its temporal persistence depending on cloud system and local conditions.

Compared to convective precipitation, research on stratiform rain has received little attention, especially from a mesoscale cloud modeling point of view. Even though the description of its microphysical and dynamical properties can be accomplished in a much easier way, its lower disaster potential seems to raise less interest in system diagnosis and predictability. However, under certain circumstances the persistence of stratiform rain may cause floods with significant damages [3].

A well known feature of stratiform rain is the melting layer due to the descent of ice particles below the freezing level [4]. The melting layer, whose thickness is generally less than 1 km, is often characterized by the so-called “bright band” corresponding to a region of increased reflectivity. While research on the radar bright band has been well documented and discussed [5]–[11], the passive microwave signature of the melting layer is not nearly as much investigated. Indeed, the complicated nature of the passive microwave signature, which is determined by surface emission and by absorption and multiple scattering of hydrometeors of different type, composition, and size spectra, is very often difficult to interpret unambiguously [12]. These aspects emphasize the ill-conditioned nature of the precipitation retrieval problem which should be approached by a detailed investigation of the forward modeling. This analysis could also suggest which *a priori* information may be useful to constrain the observable data set and improve the estimation accuracy.

In previous studies we addressed the problem of modeling the microphysical and dielectric properties of the melting layer, focusing on its impact on the simulation of microwave radiometer and radar responses from space [13]–[15]. The problem of the melting layer parameterization includes the effects of snow density, particle size distributions, and dielectric constants of mixed-phase particles. For this purpose, realistic hydrometeor profiles were taken from a two-dimensional cloud ensemble model simulating a convective-stratiform rainfall event over the East Mediterranean sea [16], [17]. The useful feature of this simulation was the availability of explicit particle mass spectra from the model which significantly reduces the number of free parameters. However, both particle size and permittivity parameterizations resulted in relative brightness temperature changes between 0–100K and reflectivity changes

Manuscript received September 20, 1999; revised February 2, 2000. This work was supported by the European Space Agency (ESA), Noordwijk, The Netherlands, Contract 9122/97/NL/NB, by Fondazione per la Meteorologia Applicata (FMA), Florence, Italy, and by the Italian Space Agency (ASI), Ispra, Italy.

F. S. Marzano is with the Dipartimento di Ingegneria Elettrica, Facoltà di Ingegneria, Università dell’Aquila, 67040 L’Aquila, Italy (e-mail: marzano@ing.univaq.it).

P. Bauer is with the Remote Sensing Data Center, German Aerospace Research Establishment (DLR), 57170 Koeln, Germany (e-mail: peter.bauer@dlr.de).

Publisher Item Identifier S 0196-2892(01)00346-1.

between 3 and 20 dBZ with respect to the control case [14], [15]. Thus, the decision for a realistic model followed the approach of excluding those parameterizations which provided unobserved signatures. This led to a selection of configurations of particle size distributions and permittivities which agreed with *in situ* observations and whose signatures simultaneously remained within realistic boundaries [14].

In this study, the simulation of the microwave radiometer and radar responses from space has been set up in view of possible applications to airborne and spaceborne observations. In particular, we have considered the channel frequencies of the advanced microwave precipitation radiometer (AMPR) and airborne rain mapping radar (ARMAR), e.g. see [18]–[20]. These sensors were extensively employed during the Tropical Ocean-Global Atmosphere Coupled Ocean-Atmosphere Response Experiment (TOGA-COARE) in 1992–93 and more recently during the Texas and Florida Underflights (TEFLUN) in 1998. Both the TOGA-COARE and TEFLUN airborne campaigns were preparatory and validation experiments, respectively, for the Tropical Rainfall Measuring Mission (TRMM). Aboard the TRMM platform launched in November 1997, the precipitation radar (PR) and the TRMM microwave radiometer (TMI) make available the same set of frequencies as ARMAR and AMPR (the 21.3-GHz channel is available on TMI only), even though AMPR operates with a different scanning geometry with respect to TMI [21].

A sensitivity analysis of spaceborne microwave passive and active retrievals of hydrometeor profiles with respect to the melting-layer parameterizations is carried out for understanding and quantifying the errors of the hydrometeor-profile retrieval, when analyzing airborne and spaceborne microwave measurements of stratiform rain events. Section II illustrates the microphysical and permittivity models of the melting layer, together with a statistical analysis of the synthetically generated data set representing airborne observations. Section III describes the inversion technique based on Bayesian principles for microwave radiometric, radar, and combined radar-radiometer retrievals. Finally, by using the generated synthetic data, Section IV discusses the numerical results in terms of statistical deviations of the retrievals including and excluding mixed-phase particle microphysical and optical properties.

## II. CLOUD MODEL AND MELTING LAYER PARAMETERIZATIONS

This section summarizes the main characteristics of the employed cloud and radiative transfer models, relevant to the sensitivity analysis presented later. For further details we refer to the paper of Bauer *et al.* [14] and Bauer and Marzano [15].

### A. Cloud Model Properties and Microphysics

The mesoscale cloud model, used in this work, is a two-dimensional (2-D) cloud ensemble model developed by Khain and Sednev [16], [17]. It is a nonhydrostatic equation system of deep convection with a computational domain covering 16 km in the vertical with a resolution of 400 m, and a horizontal size of 195 km with a resolution of 3 km. The microphysical processes included are: activation of cloud condensation (CCN) and ice nuclei; condensational growth and evaporation

of droplets; growth and sublimation of ice particles due to accretion; freezing of drops, breakup of drops and snowflakes; coalescence among drops, drops and ice particles, and among ice particles; ice multiplication, riming of snow and melting of ice. The latter does not include a prognostic budget for melting particles so that a complete exchange of ice water to liquid water in the layer below the freezing level (FL) is assumed.

For the snow density  $\rho_s$ , the cloud model assumes a constant value if  $0.01 \text{ g cm}^{-3}$ . This value is relatively low for small and moderately sized particles when compared to those reported in literature. As an alternative, we have investigated the impact of the snow density formula given by Klaassen [5]

$$\rho_s = \min[(0.7), (0.07/D_s)] \quad (1)$$

where  $\rho_s$  is in  $[\text{g cm}^{-3}]$ ,  $D_s$  [cm] denotes the diameter of a volume-equivalent spherical particle, and “min” indicates the minimum operator. The impact of (1) is such that the density of snow particles is consistently higher than  $0.01 \text{ g cm}^{-3}$ . Since the particle size distributions of the cloud model are calculated over mass spectra, the density model determines the particle size following  $m = (\pi/6)\rho_s D_s^3$ , where  $m$  [g] is the particle mass. Thus, for a given mass distribution a lower density implies bigger particles, and vice versa. For abbreviation, (1) has been called high snow-density (HSD) assumption, as opposed to the low snow-density (LSD) assumption of the original cloud model framework.

The cloud model prescribes the particle mass distributions for cloud condensation nuclei, water (raindrops and cloud droplets), ice columns, plates and dendrites, snowflakes, graupel, and hail in 33 intervals, respectively. From these, the particle size distributions (PSD) are determined assuming all particles to be spherical. To allow an evaluation of size distribution effects, all calculations were repeated for inverse-exponential PSDs because these are generally used for cloud models (e.g., [12]), which provide prognostic hydrometeor water contents rather than size spectra:

$$N(D) = N_0 \exp(-\lambda D) \quad \text{with} \quad \Lambda = [(\pi\rho N_0)/L]^{0.25}. \quad (2)$$

Here,  $N_0$  [ $\text{cm}^{-4}$ ] and  $\lambda$  [ $\text{cm}^{-1}$ ] denote the intercept (for  $D = 0$ ) and slope of  $\ln[N(D)]$ , respectively,  $D$  [cm] is the particle diameter,  $\rho$  [ $\text{g cm}^{-3}$ ] the particle density, and  $L$  [ $\text{g cm}^{-3}$ ] is the equivalent water content.  $N_0$  has been assumed fixed, so that  $L$  affects only the slope. For comparison, the explicit size spectra from the cloud model were integrated to obtain  $L$  in order to apply (2) and calculate the parameterized size spectra, as described above. Throughout the rest of the paper, the explicit particle size distributions are named EPSDs, while the parameterized ones are named PPSDs. As demonstrated in [14], the overall effect of PPSD is the underestimation (overestimation) of large (small) particle concentration. This impact will be apparent when considering the corresponding microwave signatures.

As previously mentioned, the cloud model did not include melting particle spectra due to its vertical resolution (400 m). Therefore, Bauer *et al.* in [14] introduced a sub-layer structure below the FL with a vertical resolution of 40 m employing the melting model of Mitra *et al.* [22]. This allowed the recursive computation of the meltwater mass fraction as a function of fall distance below FL and particle size and density. Since

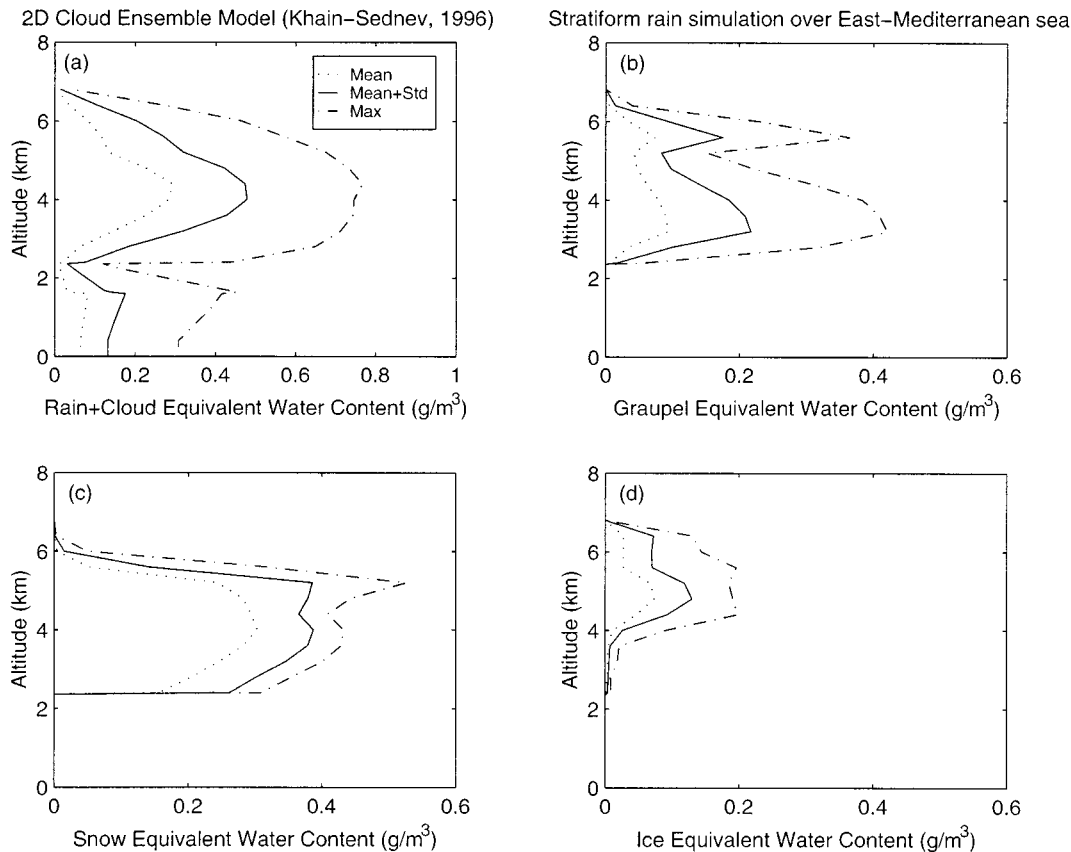


Fig. 1. Vertical profiles of average (dashed), average plus standard deviation (solid), and maximum (dash-dotted) values of equivalent water contents (EWCs) for each hydrometeor species, i.e., (a) water, (b) graupel, (c) snow, and (d) ice, derived from the cloud ensemble model simulation over the Eastern Mediterranean Sea. Only profiles with columnar rain EWCs larger than  $0.1 \text{ kg m}^{-2}$  and less than  $3 \text{ kg m}^{-2}$  (stratiform rain profiles) have been selected.

both small and less dense particles melt fastest, medium sized and moderately dense particles survive longest until complete melting. Another issue related to the insertion of a substructure was the conservation of particles fluxes at the layer boundaries. This was ensured by accounting for the available frozen water above and total rainwater below each layer [14]. It has to be stressed that very similar results in terms of meltwater mass fraction were obtained by employing a different melting layer model, developed by Rutledge and Hobbs [23].

The employed cloud model simulation describes the evolution of cloud patterns associated with coastal circulation in the Eastern Mediterranean Sea during a rain event in the cold season. The background wind induces a land-breeze type circulation. The interaction of westerly wind and coastal circulation leads to the formation of a convergence zone a few kilometers offshore and to a persistent cloud formation at this location. The clouds are transported by the wind toward the land. Precipitation formation is determined by both drops (warm rain) and melting ice particles. Thus a change of the microphysical structure from shallow convective to stratiform takes place along the storm trajectory. The freezing level was identified at 2.4 km, typical of a comparably dry environment in that maritime region.

From the considered simulation, four time steps were selected. For each time step, 67 hydrometeor profiles were available, thus obtaining 268 cloud profiles as a total. The four time steps correspond to the minutes 90, 120, 160, and 180 after the simulation starting time. These steps correspond

to mature stages of the storm and basically differ by rainfall intensity and development in the stratiform region [16]. After inserting the melting layer, the vertical resolution was finally set up at 40 m between 1.6 and 2.4 km (FL height) and to 400 m elsewhere, thus resulting in 60 layers between 0 and 16 km or 36 between 0 and 8 km. We limited our analysis to the first 8 km since all the cloud profiles throughout the chosen time steps are confined to this atmospheric portion.

As an example of the hydrometeor profile database, Fig. 1 shows the vertical profiles of the mean values, the mean values plus their standard deviations, and the maxima of the equivalent water contents (EWCs) for each hydrometeor species, i.e., water (rain+cloud), graupel, snow, and ice. Only stratiform profiles with columnar rain EWCs larger than  $0.1 \text{ kg m}^{-2}$  and less than  $3 \text{ kg m}^{-2}$  were selected to compute the statistics. The melting layer is located below the FL between 2 and 2.4 km. Graupel and snow are only present just above the FL due to the cloud model assumptions. The peak of water content around 4 km [Fig. 1(a)] is due to a concentration of supercooled cloud droplets above the FL.

### B. Permittivity Models and Radiative Transfer

Modeling the optical properties of mixed-phase particles is usually carried out by application of the classical Maxwell-Garnett or Bruggeman mixing formulas, which treat the mixture as randomly distributed inclusions in a host material or as a

symmetric mixture, respectively [24], [25]. The shortcoming of these models is that they principally imply a zero-frequency approximation thus can neither be generally applied to all sizes of particles and inclusions nor are independent of the distribution of the materials inside the particle. However, they are widely used in radar meteorology and thus the Maxwell–Garnett approach will be used as a starting point in our study. Here, we employ the Maxwell–Garnett formula ( $MG_{wi}$ ) of the first order assuming ellipsoidal inclusions of ice–air mixture in a water matrix as host material.  $MG_{wi}$  fairly well represents a water-coated particle, mostly suited for graupel at both very early and late melting stages [26]. Vice versa,  $MG_{iw}$  would represent a Maxwell–Garnett mixing formula having an ice/air matrix with water inclusions.

More recently, Meneghini and Liao developed new approaches to the problem for better representation of the particle permittivity at all melting stages and for application to higher frequencies [26]. The first method, published in 1996 and indicated here by ML96, denotes a nonlinear interpolation between Maxwell–Garnett models with either water or ice as the host material and the other as the inclusion as a function of the meltwater fraction.

A successive work of Meneghini and Liao, first appeared in 1997 and here denoted by ML97 [27], treats the particle permittivity as a summation of the permittivities of randomly distributed cells of water and ice resulting in an effective permittivity close to the average of the Maxwell–Garnett  $MG_{wi}$  and  $MG_{iw}$  models. Both models involve a numerical Fast Fourier Transfer method for the solution of the integral over the electric fields of all particle cells.

As shown by Bauer *et al.* [14], the different performances of these models at early melting stages drive the optical properties in each layer because, at later stages, many particles are either already melted or too small to produce significant effects. At the microwave frequencies relevant for precipitation retrieval (between 10 and 90 GHz),  $MG_{wi}$  always gives the largest real and imaginary parts of the complex permittivity, denoting the dominance of the water matrix contribution; vice-versa, for  $MG_{iw}$ . ML96 follows  $MG_{iw}$  for meltwater fractions below 40–50% thus resulting in weak effects comparable to those of frozen particles; its effects become significant only for very large particles. ML97 is consistently closer to  $MG_{iw}$  than to  $MG_{wi}$  and does not change much with meltwater fraction. However, at early melting stages ML97 gives higher permittivities than ML96, especially at 37 GHz, so that larger effects on the brightness temperatures of the melting layer can be expected.

In any case, the effect of permittivity model choice on the optical properties has to be viewed in conjunction with particle size distribution and snow density, which may lead to a cancellation of the net effect by opposite tendencies of the various contributions. As an example, the large permittivity of the  $MG_{wi}$  model may be suppressed when applied to small and dense particles.

For the radiative transfer calculations, an Eddington-type model was used [28]. Atmospheric absorption was derived from the Liebe model [29], while the optical parameters of spherical hydrometeors were computed by the Mie theory. The nonsphericity of particles, even though relevant for space observations at high frequencies, were considered a second-order

effect in this study. We have limited our analysis to an ocean surface because in the case of land backgrounds, the melting layer effects are almost completely obscured by the warm emissivity of land [14].

To simulate passive microwave brightness temperatures ( $T_B$ s), we chose the AMPR frequencies at 10.6, 19.3, 37.0, and 85.5 GHz with both vertical ( $V$ ) and horizontal ( $H$ ) polarizations. Attenuated radar reflectivity factors ( $Z$ s), hereinafter called simply reflectivities, were computed at 13.8 GHz thus at the same frequency of ARMAR (and PR). Multiple scattering effects were neglected, but the double-way cumulative path attenuation (CPA) and the finite layer-thickness weighting was taken into account, as illustrated by Marzano *et al.* [20]. Both  $T_B$  and  $Z$  synthetic measurements were assumed at nadir view in this work. Note that, since our atmospheric model cannot introduce depolarization, the  $V$  and  $H$   $T_B$ 's are equal even over a specular ocean background.

### III. BAYESIAN RETRIEVAL ALGORITHM

The retrieval technique, used in this work, is based on a Bayesian approach and has been already successfully applied to data from both spaceborne and airborne sensors [30]–[33]. The retrieval algorithm can be trained with a cloud-radiation database such as described in the previous section. The use of a cloud-radiation database is equivalent to the introduction of an *a priori* constraint to the inverse solution. This is the reason why a realistic and sufficiently detailed database is needed to avoid biasing the precipitation estimates when applying the inversion algorithm to real data.

Here we want to discuss some modifications to the Bayesian retrieval algorithm, which have been recently proposed for analyzing both radiometric and radar data [20]. A vector notation was chosen for brevity. Each hydrometeor profile is represented by a geophysical vector  $\mathbf{g}$  [ $\text{g cm}^{-3}$ ], consisting of EWCs for each hydrometeor species within each homogeneous layer. The vector  $\mathbf{c}$  [ $\text{kg m}^{-2}$ ] represents the columnar EWC of each hydrometeor species. The simulated multi-frequency dual-polarization brightness temperatures are indicated by a vector  $\mathbf{t}$  [K] and the attenuated multi-gate reflectivity by a vector  $\mathbf{z}$  [dBZ]. Each  $i$ th element of  $\mathbf{z}$  represents the equivalent reflectivity relative to the  $i$ th layer (i.e., range gate) reduced by the two-way path attenuation. The one-way path integrated attenuation (PIA), that is CPA from the surface to the platform, is indicated by  $A$  [dB]. The corresponding  $T_B$ ,  $Z$ , and  $A$  measurements are indicated by  $\mathbf{t}_m$ ,  $\mathbf{z}_m$ , and  $A_m$ , respectively. Considering four hydrometeor species (water, snow, graupel, and ice) in 36 layers, in general the dimensions of  $\mathbf{g}$ ,  $\mathbf{t}$ , and  $\mathbf{z}$  are 144, 8 (that is, 4 in this study: see Section II-B), and 36, respectively. Notice that many elements of  $\mathbf{g}$  are actually zero or close to zero (see Fig. 1).

#### A. Microwave Radiometer

Several approaches can be used within a Bayesian framework to derive a hydrometeor-profile content estimator [34]. An easy and effective way is based on the maximum *a posteriori* probability (MAP) criterion, which is schematically recalled hereinafter. If the total radiometric error vector  $\boldsymbol{\epsilon}_t = [\mathbf{t}_m - \mathbf{t}]$  represents the difference between measured  $\mathbf{t}_m$  and simulated  $\mathbf{t}$  from

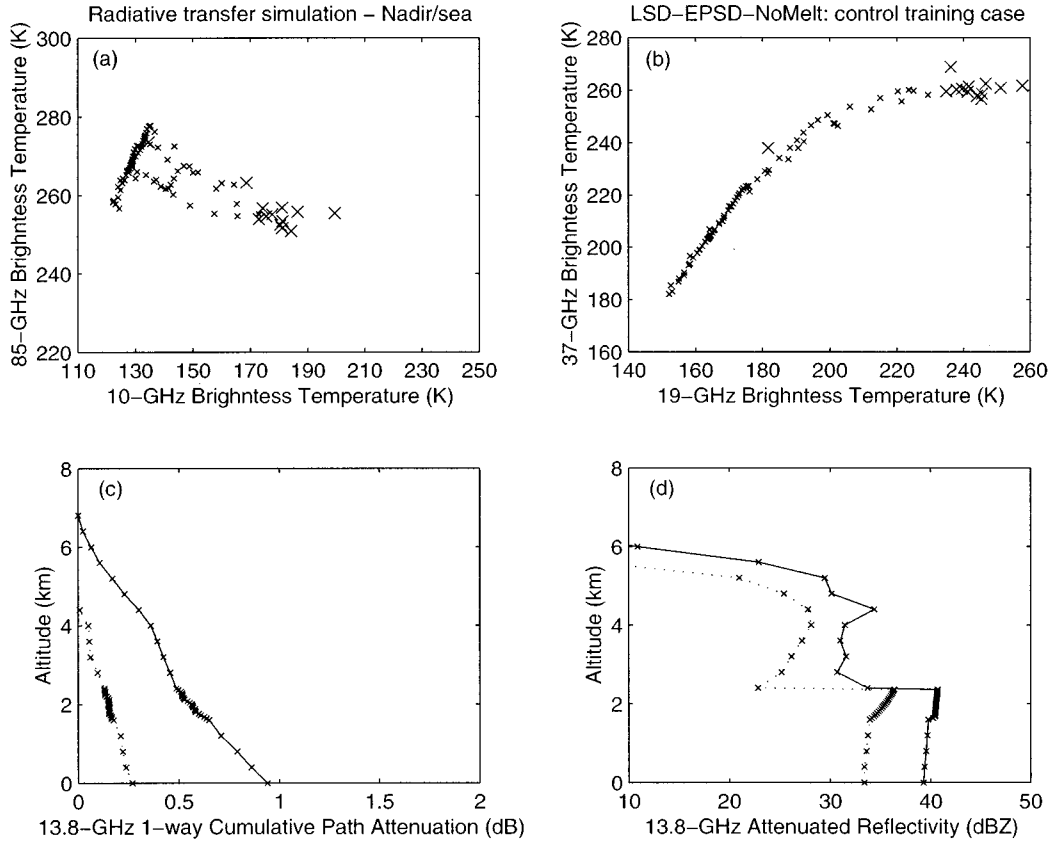


Fig. 2. Microwave signatures of the control case for the sensitivity analysis, i.e., assuming a low snow density and cloud-model explicit particle size distribution with no melting particles (LSD-EPD-NoMelt). (a) 85-GHz versus 10-GHz brightness temperature ( $T_B$ ); (b) 37-GHz versus 19-GHz  $T_B$ ; (c) cumulative nadir 1-way path integrated attenuation (PIA) at 13.8 GHz; (d) and vertical profile of attenuated nadir reflectivity at 13.8 GHz. Profiles with columnar rain EWCs larger than  $0.1 \text{ kg m}^{-2}$  have been considered. Large symbols refer to profiles with columnar rain EWCs greater than  $3 \text{ kg m}^{-2}$  (convective rain profiles).

a given profile  $\mathbf{g}$ , we can assume that  $\epsilon_t$  is due to both the instrumental noise and modeling error. A possible choice is to assume a multivariate Gaussian probability density function (PDF) both for the error  $\epsilon_t$  with a zero mean and a covariance matrix  $\mathbf{C}_{\epsilon t}$ , and for the hydrometeor vector  $\mathbf{g}$  with a mean vector  $\mathbf{m}_g$  and a covariance matrix  $\mathbf{C}_g$  [31], [20].

In our case the estimate of the covariance  $\mathbf{C}_g$  (potentially a  $144 \times 144$  element matrix) is almost impossible due to the low number of available profiles (only 268). A way to overcome this problem would have been to reduce the number of layers [20], but this would have contrasted with the fine resolution needed to characterize the melting layer itself. An alternative possibility is to relax the *a priori* information represented by  $\mathbf{g}$ , and substitute it with its integral, that is the vector  $\mathbf{c}$  of the columnar EWCs.

In previous works it was shown that the hydrometeor columnar EWCs are asymmetrically distributed [33]. Indeed, this hypothesis was verified here as well. Using numerical histograms derived from the simulation outputs considered in this work, it resulted that the maxima of water, snow, graupel, and ice columnar EWCs were  $0.4$ ,  $0.7$ ,  $0.1$ , and  $0.1 \text{ kg m}^{-2}$ , respectively, while the skewness (asymmetry) factor was  $1.2$ ,  $0.4$ ,  $1.4$ , and  $1.1$ , respectively. Notice that, since the skewness factor is the difference between the mean and modal values of the considered variate, normalized to its standard deviation, a zero skewness represents a symmetrical distribution. A

statistical test indicated that the best-fitting PDF of  $\mathbf{c}$  is the log-normal one. Thus, the random vectorial variable  $\boldsymbol{\chi}$ , defined as

$$\boldsymbol{\chi} = \ln \mathbf{c} = \ln \left[ \int_{h_1}^{h_2} \mathbf{g} \, dh \right] \quad (3)$$

follows a multivariate Gaussian PDF. Expression (3) is such that the elements of  $\boldsymbol{\chi}$  are given by the natural logarithm of the corresponding values of  $\mathbf{c}$ , that is by the integral of the hydrometeor EWCs between the heights  $h_1$  and  $h_2$ .

Therefore, the modified MAP estimation of  $\mathbf{g}$  from a radiometric measurement  $\mathbf{t}_m$  is given by maximizing the conditional probability density function  $p(\mathbf{g}|\mathbf{t}_m)$ . By simple calculations based on the Bayes rule, this maximization corresponds to the minimization of the following *radiometer modified* discriminant function  $\delta_{\text{radiom}}(\mathbf{t}_m, \mathbf{g})$  with respect to  $\mathbf{g}$

$$\delta_{\text{radiom}}(\mathbf{t}_m, \mathbf{g}) = [\mathbf{t}_m - \mathbf{t}(\mathbf{g})]^T \mathbf{C}_{\epsilon t}^{-1} [\mathbf{t}_m - \mathbf{t}(\mathbf{g})] + [\boldsymbol{\chi}(\mathbf{g}) - \mathbf{m}_{\boldsymbol{\chi}}]^T \mathbf{C}_{\boldsymbol{\chi}}^{-1} [\boldsymbol{\chi}(\mathbf{g}) - \mathbf{m}_{\boldsymbol{\chi}}] \quad (4)$$

where the superscript “ $T$ ” indicates a transposed array,  $\mathbf{m}_{\boldsymbol{\chi}}$  and  $\mathbf{C}_{\boldsymbol{\chi}}$  (with its inverse  $\mathbf{C}_{\boldsymbol{\chi}}^{-1}$ ) are the mean vector and the auto-covariance matrix of  $\boldsymbol{\chi}$ , respectively. In our case,  $\mathbf{m}_{\boldsymbol{\chi}}$  and  $\mathbf{C}_{\boldsymbol{\chi}}$  have dimension  $4 \times 1$  and  $4 \times 4$ , respectively. If the measurement

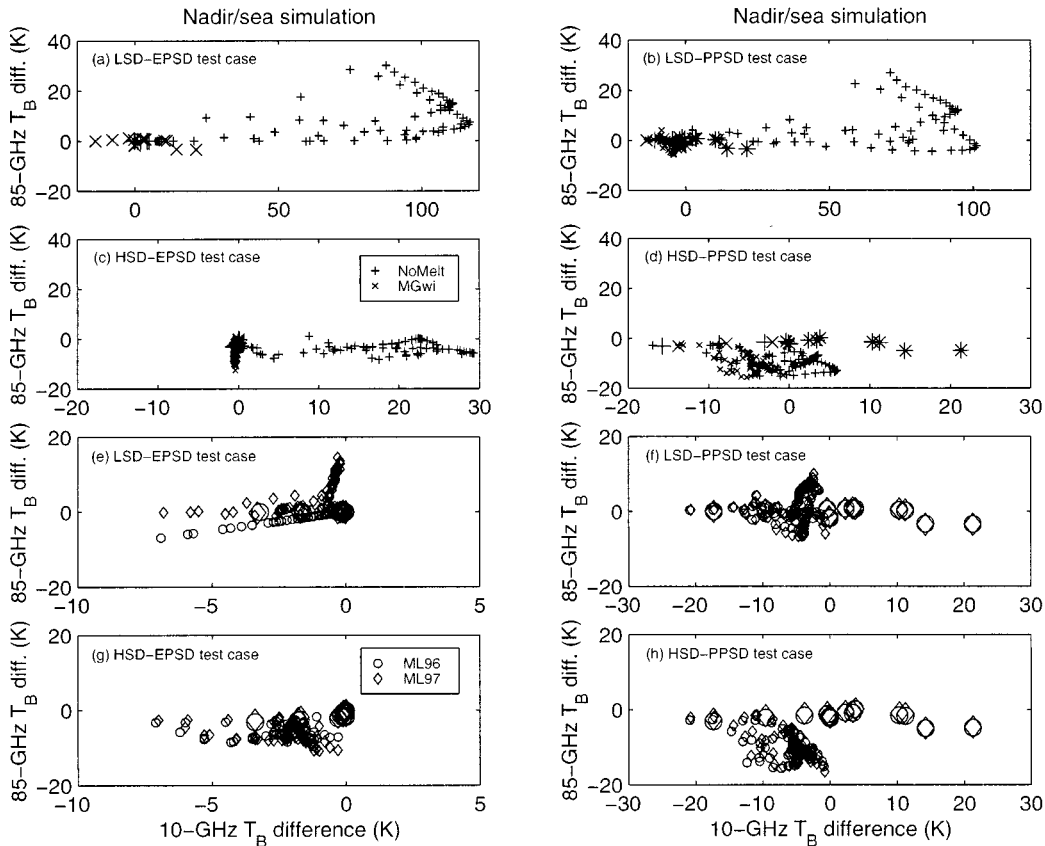


Fig. 3. Differences of simulated nadir 85-GHz versus 10-GHz  $T_B$ s with respect to the control case ones (see Fig. 2) for four model combinations, i.e., low snow density and cloud-model explicit particle size distribution (LSD-EPSPD), low snow density and parameterized particle size distribution (LSD-PPSPD), high snow density and explicit particle size distribution (HSD-EPSPD), and high snow density and parameterized particle size distribution (HSD-PPSPD). Symbols indicate permittivity model: no melting (x, NoMelt) and Maxwell–Garnett water matrix and air/ice inclusions (+, MGwi) in subplots (a)–(d), Meneghini–Liao-96 model (o, ML96) and Meneghini–Liao-97 model ( $\diamond$ , ML97) in subplots (e)–(h). As in Fig. 2, large symbols refer to convective profiles.

noise and the modeling errors are reasonably assumed to be independent, then the covariance  $\mathbf{C}_{\varepsilon t}$  can be decomposed as

$$\mathbf{C}_{\varepsilon t} = \mathbf{C}_{\varepsilon t ins} + \mathbf{C}_{\varepsilon t mod} \quad (5)$$

where the covariances  $\mathbf{C}_{\varepsilon t ins}$  and  $\mathbf{C}_{\varepsilon t mod}$  are relative to the instrumental random noise and to the forward modeling errors, respectively.

The training data set is built by a collection of simulations  $\mathbf{t}$ , while the test one is associated to a set of synthetic or experimental data  $\mathbf{t}_m$ . The term  $\mathbf{t}(\mathbf{g})$  in (4) expresses the functional dependence of  $\mathbf{t}$  on  $\mathbf{g}$  through the radiative transfer model, while  $\chi(\mathbf{g})$  reminds expression (3). The terms related to the determinant of  $\mathbf{C}_{\varepsilon t}$  and  $\mathbf{C}_{\chi}$ , as well as  $p(\mathbf{t}_m)$ , were omitted in (4) being constant in this framework [31]. The radiometric errors  $\varepsilon_t$  were assumed to be uncorrelated among the different channels having the same variance  $\sigma_{\varepsilon t}^2$ , so that from (5) the total error covariance becomes  $\mathbf{C}_{\varepsilon t} = \mathbf{I}\sigma_{\varepsilon t}^2$ , with  $\mathbf{I}$  the identity matrix. Here the total variance  $\sigma_{\varepsilon t}^2$  was set to 4 K for all channels.

### B. Combined Microwave Radiometer and Radar

The extension of the MAP criterion in (4) to the radar case is relatively easy, if we treat the radar reflectivities in the same way

as the brightness temperatures [20]. If  $\varepsilon_z$  is the reflectivity error within a range gate, it is reasonable to assume that range-gate errors are uncorrelated and Gaussian distributed with zero mean and covariance  $\mathbf{C}_{\varepsilon z}$  (e.g., this is particularly true if many samples are averaged within a gate). As already mentioned, the error  $\varepsilon_z = [\mathbf{z}_m - \mathbf{z}]$  should include the modeling error as well, that is analogously to (5)  $\mathbf{C}_{\varepsilon z} = \mathbf{C}_{\varepsilon z ins} + \mathbf{C}_{\varepsilon z mod}$ .

An interesting upgrade of the MAP estimator is the introduction of PIA as a further constraint. As an example, the so-called surface reference technique (SRT) estimates the path-integrated attenuation  $A$  from radar measurements assuming that, on a horizontal scale, any variability of the ocean surface backscattering cross-section due to surface wind, foam coverage, and raindrop impact is negligible compared to total PIA variability [36]. Thus, the total one-way path-integrated attenuation  $A$  can be derived relying on the difference between the radar near-surface measured echo in rain and rain-free regions [20].

Again, we assume that the PIA error  $\varepsilon_A$  is Gaussian-distributed with zero mean and variance  $\sigma_{\varepsilon A}^2$  together with uncorrelation between  $\varepsilon_A$  and  $\varepsilon_z$ . By applying the Bayes theorem to  $\mathbf{p}(\mathbf{g}|\mathbf{z}_m, A_m)$  and under the same assumptions valid for (4), the estimate of  $\mathbf{g}$  from measured reflectivity  $\mathbf{z}_m$  and path-integrated attenuation  $A_m$  is derived by minimizing the following

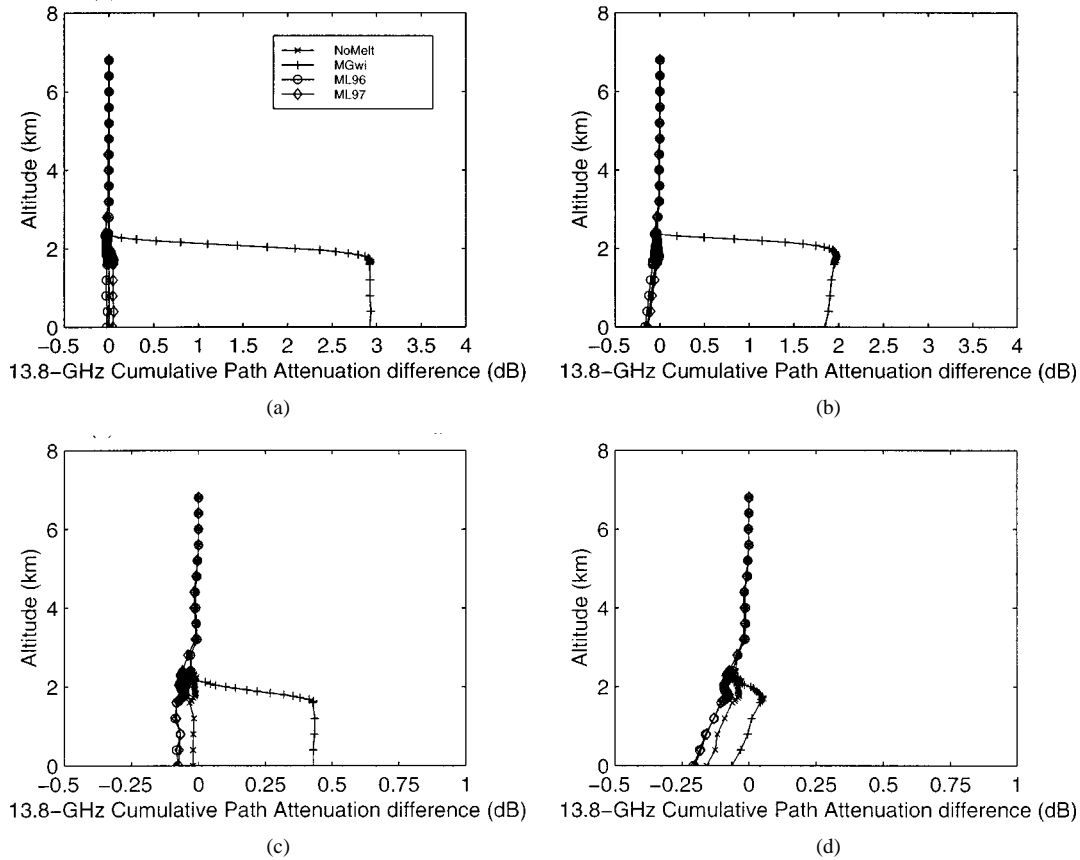


Fig. 4. Average differences of cumulative one-way cumulative path attenuation (CPA) at 13.8 GHz, computed at nadir from the cloud top, with respect to the control case ones [see Fig. 2] for (a) LSD-EPSP, (b) LSD-PDSP, (c) HSD-EPSP, and (d) HSD-PDSP and all permittivity models. As in Fig. 1, only stratiform profiles have been considered.

radar modified discriminant function  $\delta_{radar}(\mathbf{z}_m, A_m, \mathbf{g})$  with respect to  $\mathbf{g}$

$$\begin{aligned} \delta_{radar}(\mathbf{z}_m, A_m, \mathbf{g}) &= [\mathbf{z}_m - \mathbf{z}(\mathbf{g})]^T \mathbf{C}_{\varepsilon z}^{-1} [\mathbf{z}_m - \mathbf{z}(\mathbf{g})] + [A_m - A(\mathbf{g})]^2 \\ &\quad / (\sigma_{\varepsilon A}^2) + [\chi(\mathbf{g}) - \mathbf{m}_\chi]^T \mathbf{C}_\chi^{-1} [\chi(\mathbf{g}) - \mathbf{m}_\chi] \end{aligned} \quad (6)$$

where  $A(\mathbf{g})$  is the simulated PIA associated to the hydrometeor profile  $\mathbf{g}$ . Note that the introduction of path-attenuation measurements in (6) resembles the constraint of the Hitschfeld–Bordan inverse solution derived from the radar equation in an attenuating medium, widely used in spaceborne radar remote sensing [36], [37]. The specification of the covariance  $\mathbf{C}_{\varepsilon z}$  is relatively easy if its form is diagonal such that the reflectivity-error standard deviation within a range gate is proportional to the measured reflectivity (with a constant equal to the inverse of the square root of the averaged sample number for square-law detectors) [20].

In this work, the proportionality constant between the reflectivity-error standard deviation  $\sigma_{\varepsilon z}$  and the measured  $\mathbf{Z}$  has been set to 0.1 (corresponding to 100 independent samples averaged within a range gate). The standard deviation  $\sigma_{\varepsilon A}$  of the one-way total PIA error has been assumed to be 0.25 dB due to the low values of available PIAs in stratiform rain. A numerical test indicated an increase of precipitation profile retrieval accuracy up to 20% in terms of vertically-averaged root mean square error, when using the constraint  $A$  in (6).

The extension of (4) and (6) to combined radar and radiometer measurements can be accomplished by simply assuming that the errors of reflectivity, brightness temperature, and path attenuation data are statistically independent (or uncorrelated if Gaussian distributed). By applying again the Bayes theorem to  $\mathbf{p}(\mathbf{g}|\mathbf{t}_m, \mathbf{z}_m, A_m)$ , the combined estimate of  $\mathbf{g}$  is obtained from the minimization of the following *combined modified* discriminant function  $\delta_{comb}(\mathbf{t}_m, \mathbf{z}_m, A_m, \mathbf{g})$  with respect to  $\mathbf{g}$

$$\begin{aligned} \delta_{comb}(\mathbf{t}_m, \mathbf{z}_m, A_m, \mathbf{g}) &= \delta_{radiom}(\mathbf{t}_m, \mathbf{g}) + [\mathbf{z}_m - \mathbf{z}(\mathbf{g})]^T \mathbf{C}_{\varepsilon z}^{-1} \\ &\quad \cdot [\mathbf{z}_m - \mathbf{z}(\mathbf{g})] + [A_m - A(\mathbf{g})]^2 / (\sigma_{\varepsilon A}^2). \end{aligned} \quad (7)$$

The meaning of each term in (7) has been already explained before. Finally, the assumption of a Gaussian PDF for  $\mathbf{g}$  and  $\chi$ , but also for  $\mathbf{t}$ ,  $\mathbf{z}$ , and  $A$  errors, might be easily removed by using more convenient analytical PDFs.

It is worth mentioning that (7) can be directly applied only if the radar and radiometer viewing angles are the same and acquire data from the same atmospheric scenario. This is generally the case for airborne campaigns such as TOGA-COARE, where AMPR and ARMAR collected almost coincident measurements at nadir. In case of TRMM, the different scanning geometry between TMI and PR prevents a direct application of (7), and some data preprocessing or extension of the retrieval method should be carried out [37], [20].

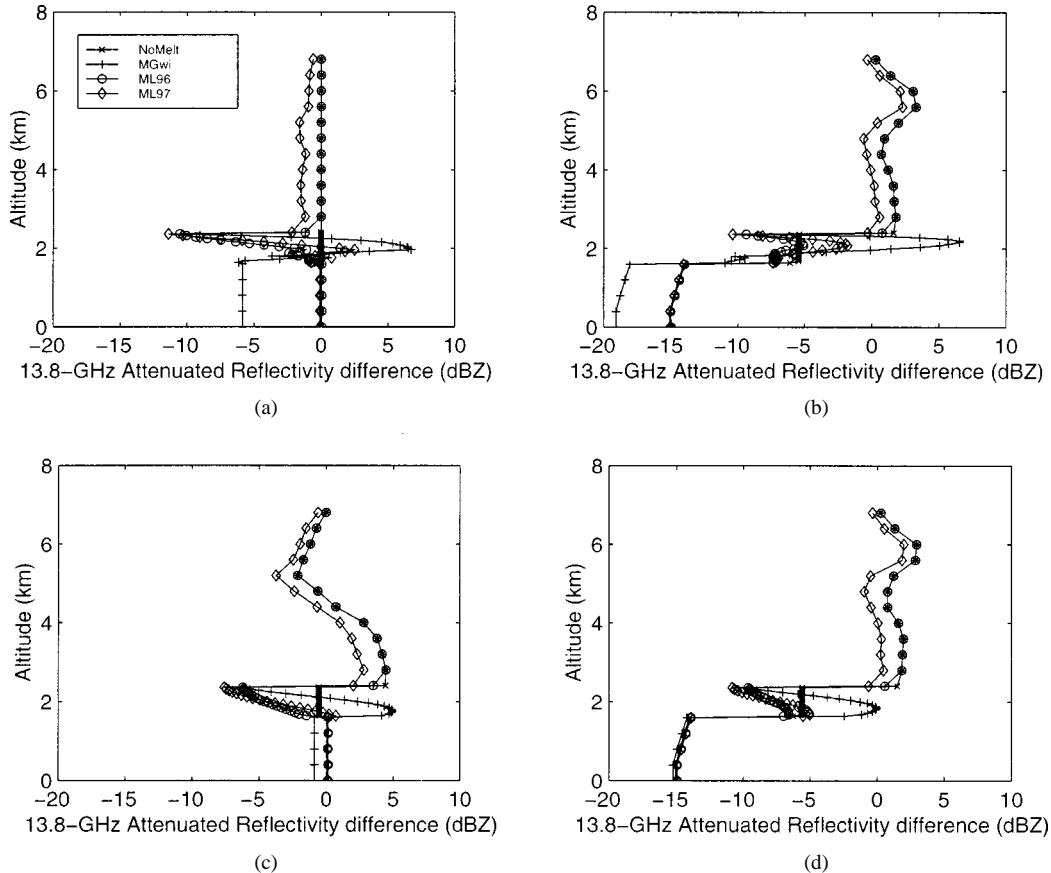


Fig. 5. As in Fig. 3, but for vertical profiles of attenuated nadir reflectivity at 13.8 GHz.

#### IV. SENSITIVITY ANALYSIS

At this stage of the work, it may be convenient to summarize the various degrees of freedom chosen in the simulation and considered in this retrieval sensitivity analysis.

- For the snow density: high (HSD) and low (LSD) values.
- For the particle size distribution: explicit (EPSD) and parameterized (PPSD) spectra.
- For the permittivity of mixed-phase particles: Maxwell–Garnett ( $MG_{wi}$ ) and Meneghini–Liao (ML96, ML97) models. We deal also with a no-melting case (NoMelt), which corresponds to the absence of any mixed-phase permittivity model within the melting layer, i.e., frozen particles are completely melted below the FL.

By permutation of snow densities and PSDs, we have four combinations for which we can show the differences among the various permittivity models in terms of  $T_B$ s and  $Z$  profiles, and their effect on hydrometeor-content profile estimate.

As said, the main goal of this study is to evaluate the sensitivity of retrieved hydrometeor profiles to the melting layer modeling perturbations. The problem of our investigation translates as follows. Suppose an application of a model-based retrieval algorithm (which was trained with the outputs of cloud model simulations) to a stratiform rain event observed from space at high spatial resolution (say 3 km) over ocean. Since the training database does not include any melting layer parameterization, we wonder how large the expected estimation error would be and how sensitive our estimate would be to the melting layer parameteriza-

tion as a function of sensor combination. In Section IV-D, we will draw some conclusions from this analysis, extending the estimation technique to a more general application.

This sensitivity is evaluated by defining a control case whose  $T_B$ s and  $Z$ s represent the training synthetic data for all other test cases based on melting parameterizations, outlined in Section II-B. This control case is given by the cloud original model framework, that is in our notation by the LSD-EPSD-NoMelt case. Fig. 2 summarizes the characteristics of the control training case in terms of signatures of 10-GHz, 19-GHz, 37-GHz, and 85-GHz  $T_B$ , together with the profiles of the average minus and plus the standard deviation of  $A$  and  $Z$  at 13.8 GHz. Only profiles with columnar rain EWCs larger than  $0.1 \text{ kg m}^{-2}$  were considered. The large symbols in the subplots refer to profiles that were classified as convective, having columnar rain EWCs above  $3 \text{ kg m}^{-2}$ . Observations are supposed at nadir over ocean.

The no-melting assumption is recognizable by the step curve of  $Z$  around the freezing level due to the discontinuous change of particle phase from liquid to ice. The average values of total PIA, i.e.,  $A$  in (6) and (7), are less than a few dB, as expected for stratiform rain. Note that the fairly good correlation between the two channels at 37-GHz and 19-GHz is typical of stratiform precipitation, and has been also experimentally observed [20]. The relatively low values of simulated high frequency  $T_B$ s for clear-air conditions (e.g., about 210 K at 85 GHz as opposed to about 240 K for TOGA-COARE) are due to the dry environment of the considered East-Mediterranean maritime region.

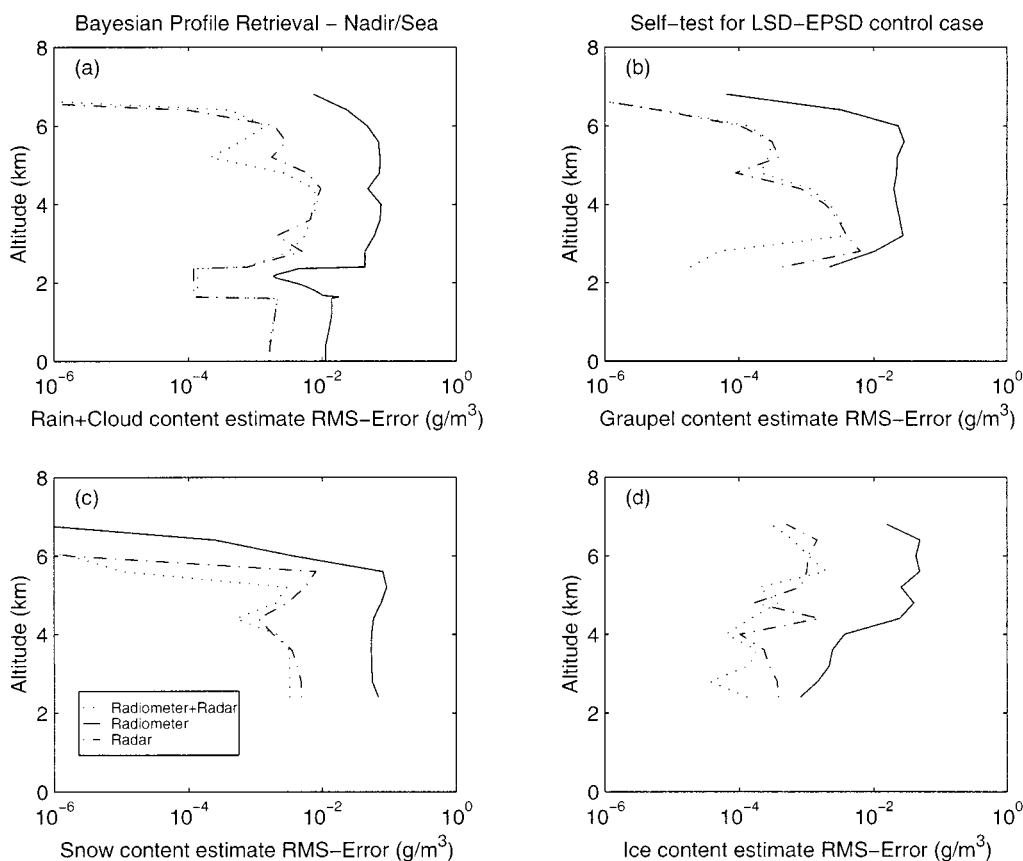


Fig. 6. Vertical profiles of root mean square (RMS) errors for rain (a) graupel, (b) snow, (c) ice, and (d) EWC estimates obtained by performing a self-test on the control case LSD-EPD-NoMelt at nadir over ocean. The solid curves refer to the use of radiometer data only (AMPR like: 10.6, 19.3, 37.0, and 85 GHz channels), the dash-dotted curves to radar data (ARMAR like: 36 range-gated reflectivities between 0 and 8 km plus total PIA at 13.8 GHz), while the dashed curves to combined radiometer plus radar data (AMPR+ARMAR like). As in Fig. 1, only stratiform profiles have been considered.

#### A. Microwave Signatures of Melting Layer

The sensitivity of the hydrometeor profile retrievals to the melting layer parameterizations will basically depend on the difference between the microwave signatures of the control case, illustrated in Fig. 2, and those derived from each parameterization (test case). Let us analyze these signatures first.

Fig. 3 shows the differences, with respect to the control case, of 85-GHz  $T_{BS}$  versus 10-GHz  $T_{BS}$  for the four possible combinations, i.e., LSD-EPD, LSD-PPSD, HSD-EPD, and HSD-PPSD, and different permittivity models, i.e., NoMelt and  $MG_{wi}$  in subplots (a)–(d), while ML96 and ML97 in subplots (e)–(h). As in Fig. 2, the large symbols refer to profiles classified as convective. Notice the different axis scales of each panel, chosen to emphasize the model comparisons. The NoMelt case will produce no differences for the LSD-EPD test, but possible deviations for all other tests due to the changes of snow density and PSD assumptions.

The effect of melting particles on  $T_{BS}$  is weak at 85 GHz with average differences less than about 15 K. For  $MG_{wi}$  and LSD cases, these differences are mainly positive up to 30 K since LSD prescribes large frozen particles which in a melting stage act radiometrically as big raindrops. For HSD and all permittivity models, the difference at 85 GHz is essentially negative due to the decrease of smaller particle emission which does not compensate for the scattering effects (producing lower  $T_{BS}$ ) [14].

At 10 GHz, large deviations occur when  $MG_{wi}$  is compared with the no-melting control case. For the  $MG_{wi}$  model, the 10-GHz  $T_{BS}$  increase by up to 120 K for the LSD case and both EPD and PSD. For the EPD test case,  $MG_{wi}$  produces relative  $T_B$  increases of about 25 K at 10 GHz. The EPD case gives rise to higher 10-GHz  $T_{BS}$  (about 20 K) than PSD ones, because the latter generally tends to underestimate the number of large particles. As predicted, ML96 does not have a great impact (<20 K at 10 GHz), while ML97 can show higher differences, especially at 85 GHz and 37 GHz (not shown).

Interestingly, the convective profiles (large symbols) are almost insensitive to the permittivity model, but fairly dependent on PSD especially at 10 GHz. Generally speaking, in the case of a convective regime, the extinction due to a larger graupel amount tends to mask the melting layer contribution. For HSD-PPSD, the underestimation (with respect to the control case) of graupel scattering above the FL and of rain and melting-particle emission below the FL gives rise to a significant net effect on 10-GHz  $T_B$  difference.

Path attenuation at 13.8 GHz plays an important role for the retrieval performance. By neglecting it, large instabilities of the inversion algorithm can be expected for both convective and stratiform precipitation [36]. Fig. 4 shows the average difference of the one-way cumulative path attenuation with respect to the control case ones for the LSD-EPD, LSD-PPSD, HSD-EPD, and HSD-PPSD combinations. The comparison among

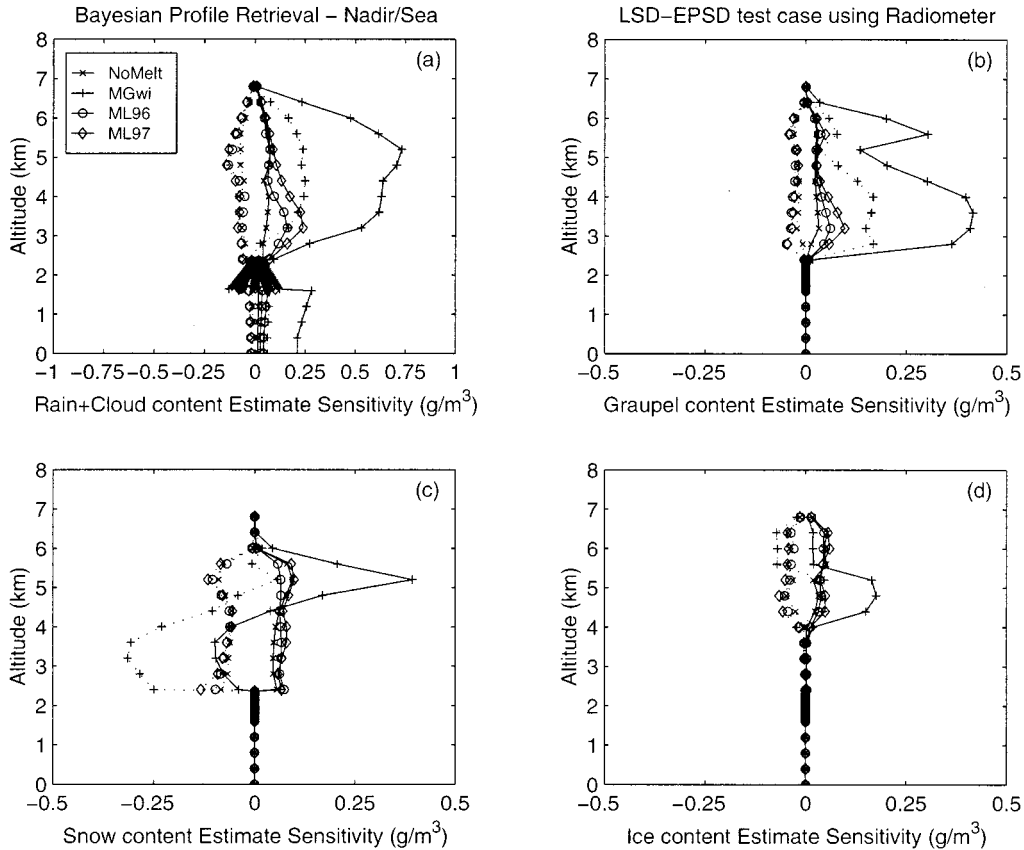


Fig. 7. Radiometric estimation sensitivity as defined by (9) for (a) rain, (b) graupel, (c) snow, and (d) ice for LSD-EPSD and all permittivity models. The solid curves refer to the lower sensitivity bound (average minus standard deviation of the error) and dashed curves refer to upper bound (average plus standard deviation of the error). As in Fig. 1, only stratiform profiles have been considered.

NoMelt,  $MG_{wi}$ , ML96, and ML97 models is carried out for stratiform-rain profiles only. In Fig. 5 the average difference of the nadir attenuated reflectivities with respect to the control case ones is shown for the same model configuration as in Fig. 4.

As expected, the peaks of  $Z_s$  are more pronounced around the melting layer, producing the typical bright band. The largest  $Z$  variability is below the FL, where the effect of path attenuation is more relevant, that is, on average up to about 3 dB for  $MG_{wi}$  and LSD cases and less than 0.5 dB for HSD cases. This also explains the high negative differences in attenuated  $Z_s$  below the FL for LSD and  $MG_{wi}$  cases. Considering the PPSD choices,  $Z$  profiles show differences larger than EPSD ones, being that CPA is generally double. Again, the  $MG_{wi}$  model denotes its strong impact in the LSD cases both in terms of  $Z$  and  $A$  variability giving rise to bright bands with maxima up 55 dB. The positive differences of  $Z$  above the FL level are basically due to a reduced cumulative path attenuation due to smaller particles as a consequence of PPSD or HSD assumptions. When using the ML96 model, the melting layer reveals a bright band relatively less than the ML97 one.

In summary, from this statistical analysis, the assumption of  $MG_{wi}$  for large and less dense snow particles seems unreasonable because it produces  $T_B$  changes, which are too high. From the numerical simulations of radar reflectivities, it results that the ML96 model does not produce significant bright bands. When reasonable model configurations are sought,  $MG_{wi}$  may be chosen for small and high dense particles (such as graupel)

and ML97 for large tenuous particles (such as snowflakes). The fact that the ML96 model agrees fairly well with numerical simulations of particle electrical properties [26] may also suggest that the role played by the melting-layer model in determining the meltwater volume fraction below the FL might be crucial. Indeed, as mentioned in Section II-B, we tried another model without obtaining significant differences.

### B. Passive Retrieval

Let us introduce a measurable quantity to evaluate the results of the sensitivity analysis. If the control case (i.e., LSD-EPSD-NoMelt) is assumed to be the training set for the considered inversion algorithms, all other combinations of melting layer parameterizations represent test cases, i.e., synthetic measurements that refer to a particular condition of the melting layer. From each of the test sets, we can estimate hydrometeor profiles  $\mathbf{g}_{est}$  by applying the Bayesian algorithms described in Section III for single and combined sensors as given in (4), (6), and (7), respectively. For each given profile  $\mathbf{g}_{con}$  of the control data set, the estimation deviation vector  $\boldsymbol{\varepsilon}_{est}$  (i.e., error profile) is given by

$$\boldsymbol{\varepsilon}_{est} = \mathbf{g}_{est} - \mathbf{g}_{con}. \quad (8)$$

An estimate sensitivity  $\mathbf{S}_{est}$ , which measures the statistical bounds of the estimation deviation vector  $\boldsymbol{\varepsilon}_{est}$ , may be introduced as follows:

$$\mathbf{S}_{est} = [\mathbf{m}_{\boldsymbol{\varepsilon}_{est}} - \boldsymbol{\sigma}_{\boldsymbol{\varepsilon}_{est}}, \mathbf{m}_{\boldsymbol{\varepsilon}_{est}} + \boldsymbol{\sigma}_{\boldsymbol{\varepsilon}_{est}}] \quad (9)$$

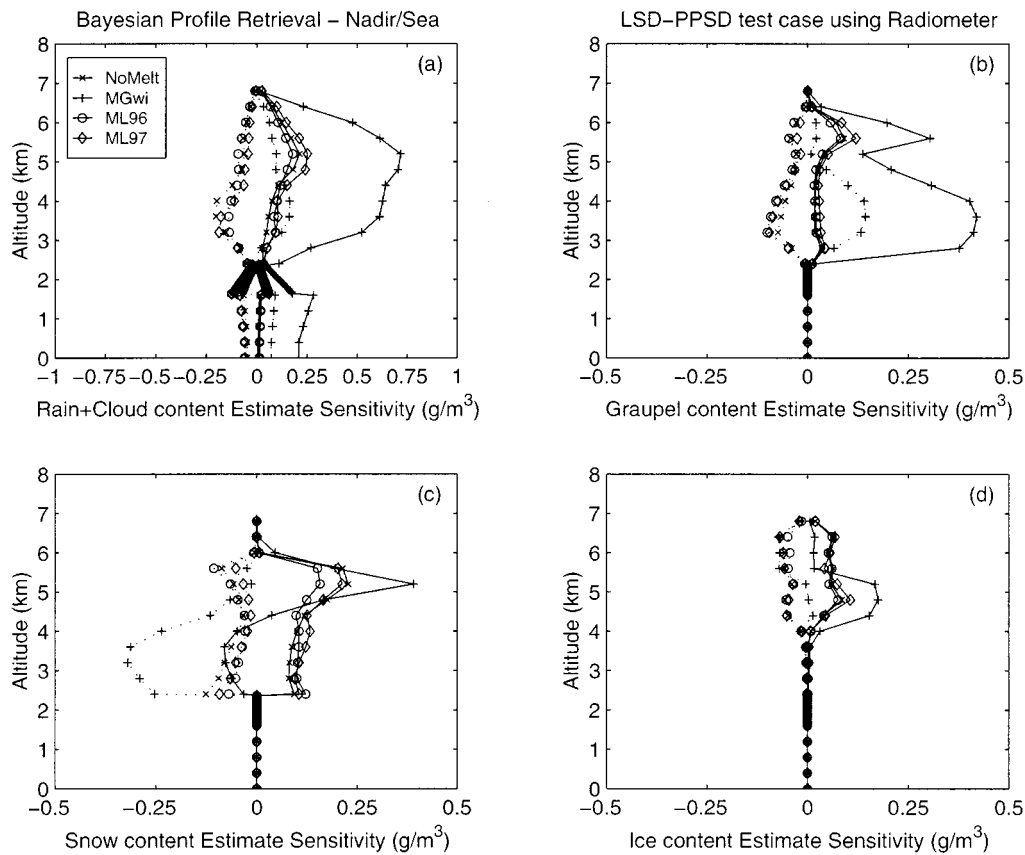


Fig. 8. As in Fig. 7, but for the LSD-PPSD test data set.

where  $\mathbf{m}_{est}$  and  $\sigma_{est}$  are the mean and standard deviation vectors of  $\boldsymbol{\varepsilon}_{est}$ , computed over the available hydrometeor profiles of the training data set. Indeed, the estimate sensitivity can be interpreted as a retrieval error indicator considering also that the test data set is independent from the training one. To avoid ambiguities and solely interpret melting particle signatures, the convective profiles (as defined in Section IV-A, see Fig. 2), as well as the clear-air profiles, were excluded from the retrieval analysis.

A preliminary self test of proposed retrieval algorithms can give an idea of the expected accuracies. Fig. 6 shows the root mean square (RMS) errors for the retrieval of water, graupel, snow, and ice profiles, obtained by performing a self test on the control case LSD-EPSPD-NoMelt at nadir over ocean. The solid curves refer to the use of radiometer data only (AMPR like), while the dash-dotted curves to radar data only (ARMAR like). The dashed curves apply to radiometer plus radar data (AMPR+ARMAR like) which will be discussed in the next section. We recall that the measurement vector  $\mathbf{t}_m$  has dimension 4 (i.e., using 10.6, 19.3, 37.0, and 85 GHz), since the  $V$  and  $H$  signatures are equal at nadir.

Since it is a self test, the errors of Fig. 6 represent an optimistic evaluation, in other words, a lower bound of the expected RMS errors. Nevertheless, these results show that the RMS errors are less than  $0.1 \text{ g m}^{-3}$  (less than 30% in terms of fractional percentage error), being higher for water and graupel profiles. It is interesting to point out that, if the convective profiles have been taken into account, the RMS errors would have increased up to  $0.2 \text{ g m}^{-3}$ , especially in the rain and cloud liquid layers.

A first plot of  $\mathbf{S}_{est}$  is given in Fig. 7, which illustrates the radiometric estimate sensitivity of rain, graupel, snow, and ice equivalent water contents for the LSD-EPSPD test case, when using the No-melting,  $MG_{wi}$ , ML96, and ML97 permittivity models. Note the different  $x$ -axis scale for panel (a).

The highest estimate sensitivity is produced for rain and graupel (overestimation up to  $0.75$  and  $0.4 \text{ g m}^{-3}$ , respectively) for the  $MG_{wi}$  case, followed by ML97, as a consequence of the large differences in the  $T_B$  space, as observed in Figs. 3 and 5. The sensitivity in the melting layer increases with the distance from the FL for rain profiling. The anomalous sensitivity curve for snow retrieval, with a tendency to underestimate below 4.5 km and to overestimate above 4.5 km, is likely due to the retrieval algorithm trying to find an unusual combination of rain and nonmelting ice profiles (which explain the increased emission and spectral response due to melting). By comparing Fig. 7 with Fig. 6, it is worth mentioning that the estimate sensitivity can be ten times higher than RMS errors for all hydrometeor profile retrieval. If we take into account the possible contamination of convective profiles, that is we include the latter into the training and the test data set, the resulting sensitivity can be up 30 times worse than the self test RMS errors. Notice that the combination of  $MG_{wi}$  with LSD was already identified to be fairly unrealistic in the previous section.

Fig. 8 draws a picture similar to Fig. 7 for the LSD-PPSD test case. Even though PPSDs tend to reduce the concentration of large particles, the results are not too much different for  $MG_{wi}$  due to its general exaggeration of the melting layer emission for

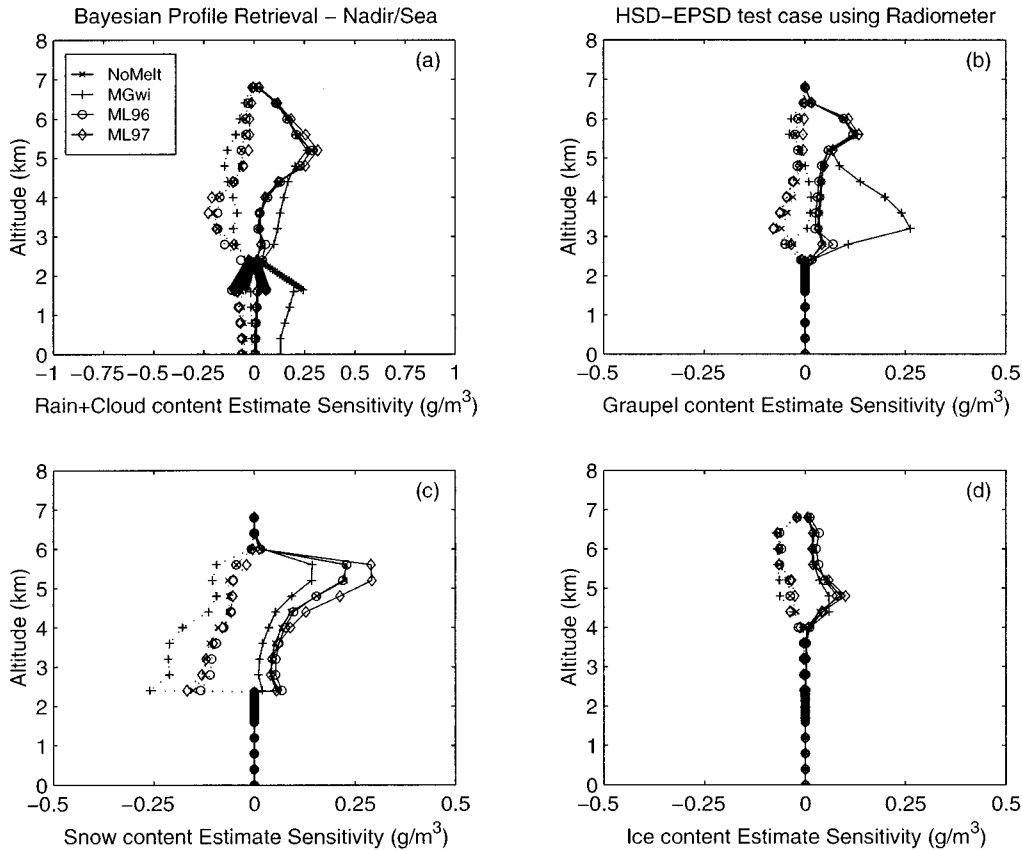


Fig. 9. As in Fig. 7, but for the HSD-EPSPD test data set.

large particles with low densities. However, the ML97 case is rather sensitive to the particle spectra model so that, for relatively small particles (i.e., PPSD case), the retrieval sensitivity is reduced by a factor of 2 below the FL. On the contrary, the change of PSD shows a little effect on the ML96 sensitivity.

The results change when the LSD assumption is replaced by the HSD one, as shown in Fig. 9. Here, smaller particles with higher densities reduce the excess scattering and extinction in the melting layer and therefore, diminish the impact of the permittivity models. The sensitivities are even reduced for rainwater when  $MG_{wi}$  is applied, with a minor effect on the other hydrometeor species. The fact that 85-GHz  $T_B$  values are basically less than the control case ones (see Fig. 2) is responsible for the modification of the snow sensitivity curve when compared to those of Figs. 7 and 8.

Finally, from Fig. 10 when PPSDs are used together with HSD assumption, the lower concentration of larger particles further reduces the differences between the permittivity models. In this case, the anomalous behavior due to the  $MG_{wi}$  model is no more observed even for rain and graupel profiles. From a retrieval point of view, this is the best situation with sensitivities no greater than  $0.3\text{--}0.4\text{ g m}^{-3}$ , which are indeed still four to five times greater than the self-test RMS errors given in Fig. 6.

### C. Combined Retrieval

The advantage to use a multisensor retrieval scheme for precipitation retrieval has already been demonstrated in literature [6], [20], [33], [37]. A further confirmation of this is given in

Fig. 6, where the RMS error profile is plotted, obtained by applying (6) and (7) to radar data and combined radiometer plus radar data, respectively (e.g., AMPR plus 36 range-gated reflectivities plus PIA at 13.8 GHz).

As known, the contribution of Ku-band radar data helps the microwave radiometer in improving the accuracy of large and dense particle retrieval, such as raindrops and graupel. As seen from the figure, the improvement can be higher than 50%. The use of radar data only gives results slightly worse than the combined ones, especially for cloud liquid water above the FL, and graupel content below 4 km, where the radiometer information is more effective in the retrieval synergy. However, consider that these results are only theoretical since for radar data, we presumed to know exactly the vertical profiles of the reflectivity-rainrate ( $Z-R$ ) relation. Indeed, in real applications, the  $Z-R$  variability and unpredictability is a major source of uncertainty.

The effect on the estimate sensitivity when implementing a combined radar-radiometer retrieval, instead of a radiometer-only retrieval, is illustrated in both Fig. 11, which is analogous to Fig. 7 for LSD-EPSPD, and Fig. 12, which is analogous to Fig. 10 for HSD-PPSD. The other cases, corresponding to Figs. 8 and 9, are not shown for brevity.

For LSD-EPSPD (Fig. 11), the radar provides a contribution to the reduction of the estimate sensitivity by slightly, narrowing the uncertainty close to that of the control case for all permittivity models, especially for  $MG_{wi}$  below the FL. The sensitivity reduction in the rain layers is also accompanied by a reduction in the cloud-liquid layers due to the constraints imposed

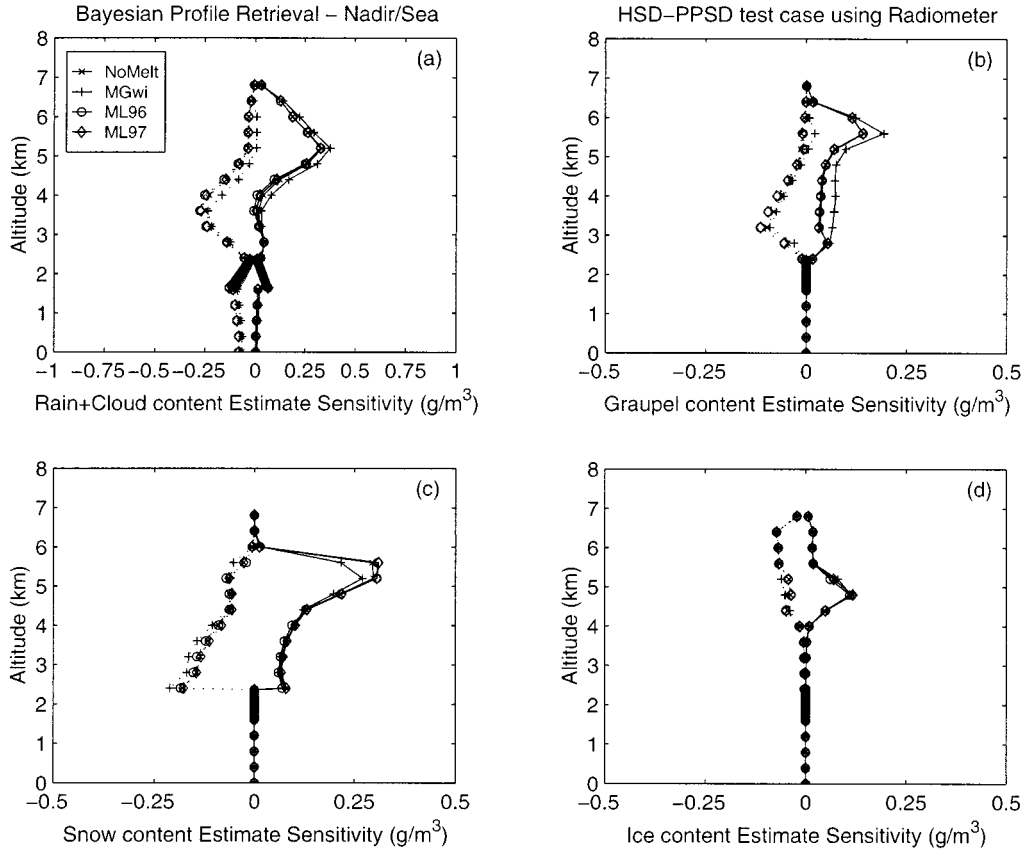


Fig. 10. As in Fig. 7, but for the HSD-PPSD test data set.

by the cloud model itself in terms of hydrometeor vertical profiles. A further sensitivity reduction is obtained for HSD-PPSD (Fig. 12), where the retrieval results are almost insensitive to the chosen permittivity model. In this case, the maximum values of  $S_{est}$  are still almost double with respect to the self-test RMS error ones given in Fig. 6.

Finally, notice that, if convective profiles were also considered in the considered retrieval tests, the estimate sensitivity could have been degraded of ten times with respect to the self-test RMS errors. The intuitive explanation is that in this circumstance, the training set does not have any information about cloud structure in convection regimes.

#### D. Implications for Real Data Applications

The results shown in the previous sections put in evidence the need to include a melting layer characterization within the training database in order to reduce the estimate sensitivity, and thus the retrieval error. In practical applications of retrieval techniques to airborne data, one could include either the most probable melting layer model in the training set (e.g., see Section IV-A) or simulations based on several melting models if there is no significant evidence to support the use of one melting model over another. The reason for the latter choice is that the precipitation profile estimates would not be biased due to an incomplete training data set. Moreover, in naturally occurring melting layers, there might be an intrinsic variability of particle dielectric properties, densities, and size distributions that would indicate the need for a broader training set.

The aforementioned approach can be translated into a further formulation of the Bayesian inversion algorithm based on MAP criterion. Considering, for example, the modified combined retrieval given in (7), we can introduce the melting model configuration  $k$  so that to each cloud profile  $\mathbf{g}$  it is possible to associate a corresponding set of simulated brightness temperatures  $\mathbf{t}^{(k)}$ , reflectivity  $\mathbf{z}^{(k)}$ , and path-integrated attenuation  $A^{(k)}$ . By listing all combinations illustrated in this work (including the no-melting case), it results that the total number  $N_c$  of melting model configurations is  $2 \times 2 \times 4 = 16$ . Thus, from the Bayes theorem applied to the conditional PDF  $p(\mathbf{g}, k | \mathbf{t}_m)$ , it follows:

$$\begin{aligned} p(\mathbf{g}, k | \mathbf{t}_m) &= p(\mathbf{t}_m | \mathbf{g}, k) p(\mathbf{g}, k) / p(\mathbf{t}_m) \\ &= p(\mathbf{t}_m | \mathbf{g}, k) p(\mathbf{g} | k) P(k) / p(\mathbf{t}_m) \end{aligned} \quad (10)$$

where  $P(k)$  is the discrete probability of the  $k$ th melting model configuration. As usual, we can interpret  $p(\mathbf{t}_m | \mathbf{g}, k)$  as the PDF of the  $k$ th model  $T_B$  error  $\varepsilon_t^{(k)}$ , that is,  $p(\mathbf{t}_m | \mathbf{g}, k) = p(\varepsilon_t^{(k)}) = p(\mathbf{t}_m - \mathbf{t}^{(k)}(\mathbf{g}))$ . Moreover, since the profiles  $\mathbf{g}$ , belonging to the  $k$ th model configuration, are the same for each configuration, we can assume that  $p(\mathbf{g} | k) = p(\mathbf{g})$ , or better, as done in (3), substitute  $p(\mathbf{g})$  with  $p(\chi)$ . Considering that  $p(\mathbf{t}_m)$  is constant with respect to  $\mathbf{g}$ , as for (4), under the assumption of Gaussian PDFs for both  $\varepsilon_t^{(k)}$  and  $\chi$ , the *generalized radiometer* discriminant function  $\delta_{radiomG}(\mathbf{t}_m, \mathbf{g}, k)$  to be minimized with respect to  $\mathbf{g}$  and  $k$  is

$$\begin{aligned} \delta_{radiomG}(\mathbf{t}_m, \mathbf{z}_m, A_m, \mathbf{g}, k) &= [\mathbf{t}_m - \mathbf{t}^{(k)}(\mathbf{g})]^T \mathbf{C}_{et}^{-1} [\mathbf{t}_m - \mathbf{t}^{(k)}(\mathbf{g})] + [\chi(\mathbf{g}) - \mathbf{m}_\chi]^T \\ &\quad \cdot \mathbf{C}_\chi^{-1} [\chi(\mathbf{g}) - \mathbf{m}_\chi] + P(k) \quad \text{with } k = 1 \div N_c. \end{aligned} \quad (11)$$

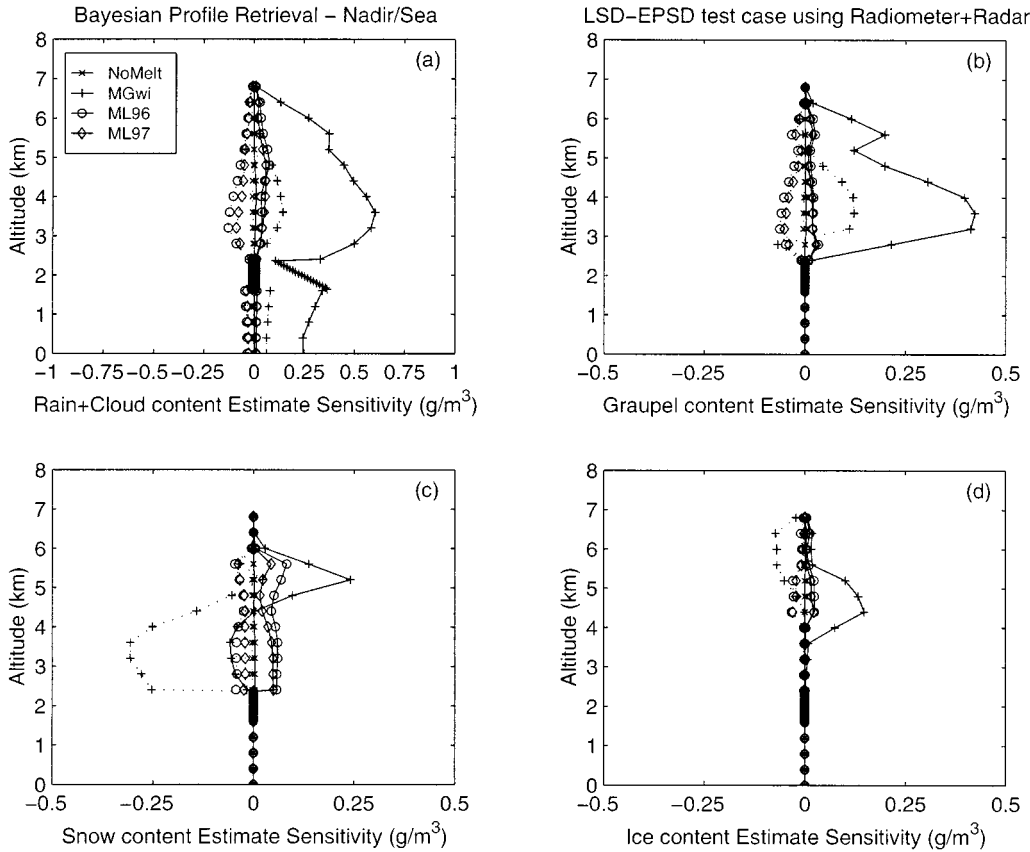


Fig. 11. As in Fig. 7, but for the *combined* Bayesian retrieval algorithm applied to combined radiometric and 13.8-GHz radar synthetic data at nadir over the sea.

The extension of (11) to the *generalized combined* discriminant function  $\delta_{combG}(\mathbf{t}_m, \mathbf{z}_m, A_m, \mathbf{g}, k)$  is straightforward. Similarly to (7), it holds

$$\begin{aligned} \delta_{combG}(\mathbf{t}_m, \mathbf{z}_m, A_m, \mathbf{g}, k) &= [\mathbf{t}_m - \mathbf{t}^{(k)}(\mathbf{g})]^T \mathbf{C}_{\varepsilon t}^{-1} [\mathbf{t}_m - \mathbf{t}^{(k)}(\mathbf{g})] \\ &+ [\mathbf{z}_m - \mathbf{z}^{(k)}(\mathbf{g})]^T \mathbf{C}_{\varepsilon z}^{-1} [\mathbf{z}_m - \mathbf{z}^{(k)}(\mathbf{g})] \\ &+ [A_m - A^{(k)}(\mathbf{g})]^2 / (\sigma_{\varepsilon A}^2) + [\boldsymbol{\chi}(\mathbf{g}) - \mathbf{m}_{\chi}]^T \mathbf{C}_{\chi}^{-1} \\ &\cdot [\boldsymbol{\chi}(\mathbf{g}) - \mathbf{m}_{\chi}] + P(k) \quad \text{with } k = 1 \div N_c. \quad (12) \end{aligned}$$

In (11) and (12), the probability  $P(k)$  weights each configuration and might be chosen in accordance with the observed atmospheric scenario and available *a priori* information. If no melting model is preferred, then  $P(k)$  can be assumed uniform in order not to contribute to the discriminant function minimization. In principle, in (11) and (12) even  $\mathbf{C}_{\varepsilon t}$ ,  $\mathbf{C}_{\varepsilon z}$ , and  $\sigma_{\varepsilon A}$  could depend on the  $k$ th melting-model configuration. In this case, their determinants should be included in the formulas [31].

It is expected that the use of the generalized combined algorithm should reduce the estimate sensitivity, that is, the retrieval errors. In order to prove it, we can set up another numerical experiment slightly different from the previous ones. As a training data set, we can use all outputs of the first three time steps of the simulation (i.e., minutes 90, 120, and 160). It means using  $16 \times 67 \times 3 = 3216$  data that describe the radiate transfer outputs in terms of  $\mathbf{t}^{(k)}$ ,  $\mathbf{z}^{(k)}$ , and  $A^{(k)}$ . For a simple independent test, we can select the outputs from the remaining time step (i.e., minute

180), which is not included in the training set. The test data set can be also grouped with respect to snow density, size distribution, and dielectric models as done in Figs. 8–12.

Let us consider the *generalized* radiometer retrieval algorithm, as given in (11). As an example, Fig. 13 shows the obtained results in a way analogous to Fig. 7 for the LSD-EPSD test case. Note that this case was the one with the largest estimate sensitivities. As expected, the estimate sensitivity (retrieval error) is much less than the one derived by using a no-melting training data set. The exaggerated sensitivity due to the Maxwell–Garnett  $MG_{wi}$  model is significantly reduced, since this variability was introduced in the training data. The retrieval RMS error is less than  $0.15 \text{ g m}^{-3}$  for all hydrometeors, being higher above the FL. For brevity, we do not show the other test cases as the conclusions are similar to those illustrated for Fig. 13.

Before concluding this section, we have to point out the importance of performing a discrimination between stratiform and convective rainfall before applying the proposed algorithms. The same numerical experiment, illustrated in Fig. 13, would have given much worse results if convective profiles have been included in the test data set. Recent studies published in the literature have shown that a classification of stratiform versus convective precipitation can be carried out by spaceborne radar and radiometer data [21], [38], [39]. It is worth mentioning that, by considering a dual-step cascade algorithm (first classify then retrieve), the overall retrieval error probability is given by the multiplication of the error probability associated with each retrieval step.

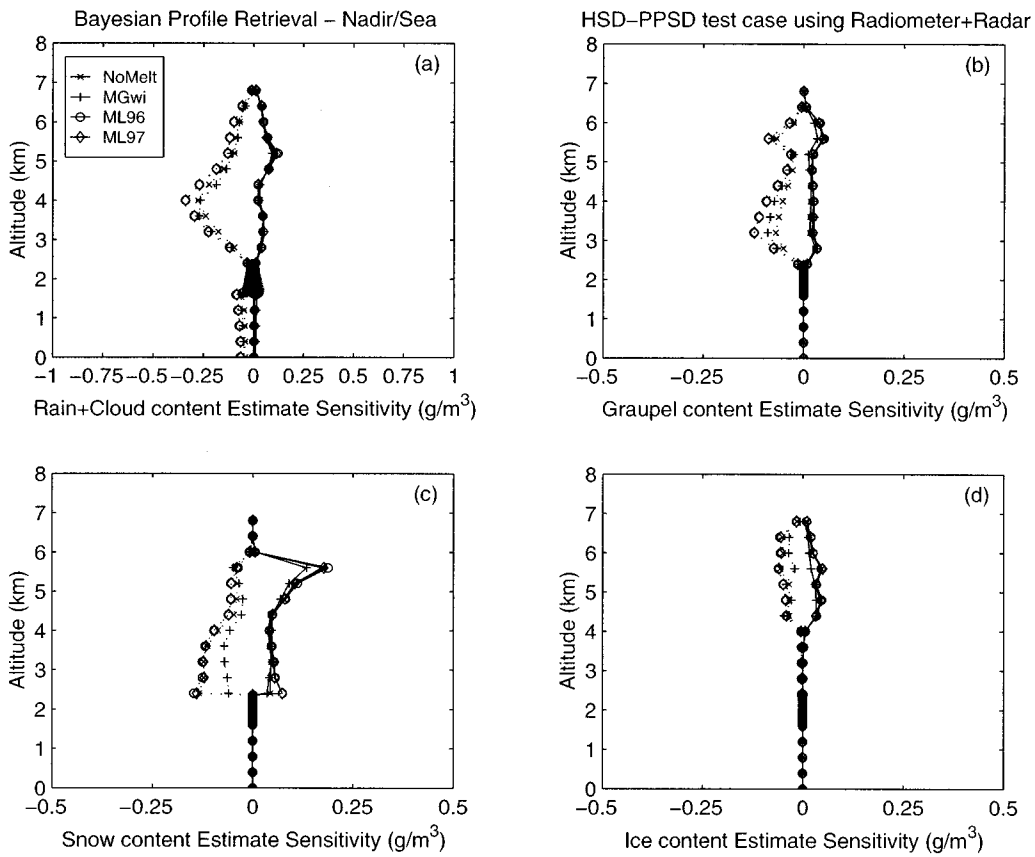


Fig. 12. As in Fig. 10, but for the *combined* Bayesian retrieval algorithm applied to combined radiometric and 13.8-GHz radar synthetic data.

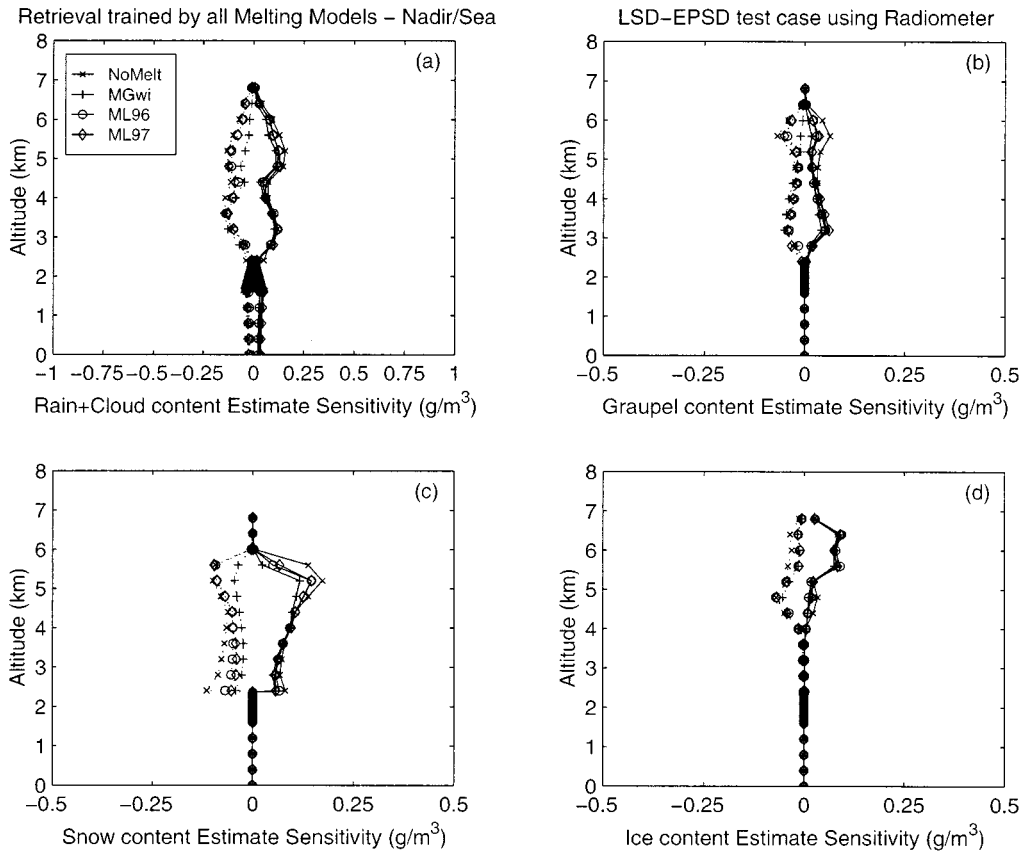


Fig. 13. As in Fig. 7, but for the *radiometric* Bayesian retrieval algorithm trained by all melting model data sets derived from the first three available time steps (minutes 90, 120, and 160) of the cloud model simulation and tested using the cloud profiles taken from remaining time step (minute 180).

## V. CONCLUSIONS

A sensitivity analysis of airborne microwave passive and active retrieval of hydrometeor profiles to the melting layer parameterization was carried out using synthetic data. This work started from the results of a previous study, where a forward radiative transfer model of stratiform rain, including mixed-phase particle effects, was developed. The parameterizations of the melting layer included the effects of snow density and particle size distributions of liquid and ice hydrometeors, as well as various dielectric models for melting particles. The hydrometeor profiles were derived from a two-dimensional (2-D) cloud ensemble model simulating a stratiform rainfall over the East Mediterranean sea.

The statistical analysis of the cloud radiative data set has revealed that the assumption of the  $MG_{wi}$  model for large and less dense snow particles seems unreasonable since too high variations of  $T_B$  are produced. On the other hand, from radar reflectivity simulations the ML96 model does not yield significant bright bands. When looking for reasonable configurations of permittivity models, the  $MG_{wi}$  formula may be chosen for small and high dense particles like graupel particles, while the ML97 model for large tenuous particles like snowflakes. Indeed, applying the ML97 model to both graupel and snow might be a good compromise as well, mainly dependent on the amounts of the two hydrometeors.

Airborne remote sensing techniques based on microwave radiometric, radar, and combined radar-radiometer data were also considered within a Bayesian inversion framework. The maximum *a posteriori* probability criterion was used with a new *a priori* constraints derived from the columnar hydrometeor contents of the cloud model and from the measured path integrated attenuation. The algorithms were applied to nadir observations over ocean, since over land the melting layer showed negligible effects on brightness temperatures.

Numerical results were shown in terms of statistical deviations of the retrieved profiles with respect to a control case, defined as the one using the cloud-model PSD and snow density without a melting layer implemented. The idea was to simulate the application of a model-based retrieval algorithm (trained with the outputs of cloud model simulations) to a stratiform rain event observed from space at high spatial resolution over ocean. Since the training database was supposed not to include any melting-layer parameterization, the expected estimate error was interpreted as a retrieval sensitivity to each melting layer parameterization as a function of the sensor combination.

A significant impact of snow density and PSD choices was noted. When using a radiometer only, for the HSD-PPSD case (which implies an increase of smaller particle concentration), the estimated sensitivity was found four to five times greater than the self-test RMS errors. On the opposite, in case of LSD-EPSD, the sensitivity itself was as high as ten times. When using combined radar-radiometer data, the sensitivity slightly reduced, being almost insensitive to the chosen permittivity model in the HSD case. It should be also considered that the presence of convective profiles in the test data set can drastically degrade the retrieval results.

It was also found that opposite effects due to different models tend to balance each other (as in the case of sensitivity increase

due to  $MG_{wi}$  model counterbalanced by the sensitivity decrease due to the introduction of HSD parameterization). This suggests that the analysis of measured airborne and spaceborne data could not resolve these ambiguities unless *in situ* or other source measurements are available. As an implication for real data applications, we argued that a strategy for stratiform rainfall retrieval could be to randomize the training data set by including all physically reasonable melting models. Numerical results, derived by carrying out a simple numerical experiment, tended to confirm this conclusion. Note that a previous separation between stratiform and convective precipitation is of primary importance for applying the proposed Bayesian algorithms.

The available cloud model simulation, which referred to a very dry maritime environment, prevented us from applying the model-based retrieval algorithms to real data such as those from TOGA-COARE or TEFLUN campaigns. Unlike the retrieval algorithms based on optimization techniques such as those in [36], [37], the cloud-model based approach needs a pregenerated cloud radiative database, physically consistent with the observed atmospheric scenario. In the case of tropical cyclones, the freezing level is generally around 4.5 km [20], much higher than the 2.4 km of our cloud model. Further work will be devoted to construct a cloud radiative database for tropical stratiform rain events to be used with both airborne and spaceborne data.

## ACKNOWLEDGMENT

The authors wish to thank the reviewers for their careful reading of the paper and their helpful suggestions to improve this study. They also wish to thank Dr. A. Khain for providing the cloud model simulations and many comments on their utilization as well, and Dr. P. Baptista and Dr. A. Mugnai for their general support on this subject.

## REFERENCES

- [1] R. A. Houze, "Structures of atmospheric precipitation systems: A global survey," *Radio Sci.*, vol. 16, pp. 671–689, 1981.
- [2] —, "Stratiform precipitation in regions of convection: A meteorological paradox?," *Bull. Amer. Meteorol. Soc.*, vol. 78, pp. 2179–2196, 1997.
- [3] G. Boni, M. Conti, S. Dietrich, L. Lanza, F. S. Marzano, A. Mugnai, G. Panegrossi, and F. Siccardi, "Multisensor observations during the event of November 4–6, 1994 over Northern Italy," *Remote Sensing Rev.*, vol. 14, pp. 91–117, 1996.
- [4] L. J. Battan, *Radar Observations of the Atmosphere*. Chicago, IL: Univ. Chicago Press, 1973.
- [5] W. Klaassen, "Radar observations and simulation of the melting layer of precipitation," *J. Atmos. Sci.*, vol. 45, pp. 3741–3753, 1988.
- [6] J. L. Schols and J. A. Weinman, "Retrieval of hydrometeor distribution over the ocean from airborne single-frequency radar and multi-frequency radiometric measurements," *Atmos. Res.*, vol. 34, pp. 329–346, 1994.
- [7] W. Zhang, S. I. Karhu, and E. T. Salonen, "Predictions of radiowave attenuation due to a melting layer of precipitation," *IEEE Trans. Antennas Propagat.*, vol. 42, pp. 492–499, 1994.
- [8] D. S. Zrnica, R. Raghavan, and V. Chandrasekhar, "Observations of copolar correlation coefficient through a bright band at vertical incidence," *J. Appl. Meteorol.*, vol. 33, pp. 45–52, 1994.
- [9] R. Meneghini, H. Kumagai, J. R. Wang, T. Iguchi, and T. Kozu, "Microphysical retrievals over stratiform rain using measurements from an airborne dual-wavelength radar-radiometer," *IEEE Trans. Geosci. Remote Sensing*, vol. 35, pp. 487–506, Mar. 1997.
- [10] S. L. Durden, A. Kitiyakara, E. Im, A. B. Tanner, Z. S. Haddad, F. K. Li, and W. J. Wilson, "ARMAR observations of the melting layer during TOGA-COARE," *IEEE Trans. Geosci. Remote Sensing*, vol. 35, pp. 1453–1456, 1997.

- [11] M. M. G. D'Amico, A. R. Holt, and C. Capsoni, "An anisotropic model of the melting layer," *Radio Sci.*, vol. 33, pp. 535–552, 1998.
- [12] A. Mugnai, E. A. Smith, and G. J. Tripoli, "Foundations for statistical-physical precipitation retrieval from passive microwave satellite measurements. Part II: Emission source and generalized weighting function properties of a time-dependent cloud-radiation model," *J. Appl. Meteorol.*, vol. 32, pp. 17–39, 1993.
- [13] P. Bauer, J. P. V. Poiaries Baptista, and M. de Iulio, "On the effect of the melting layer on the microwave emission of clouds over the ocean," *J. Atmos. Sci.*, vol. 56, pp. 852–867, 1999.
- [14] P. Bauer, A. Khain, I. Sednev, R. Meneghini, C. Kummerow, F. S. Marzano, and J. P. V. Poiaries Baptista, "Combined cloud-microwave radiative transfer modeling of stratiform rainfall," *J. Atmos. Sci.*, vol. 57, pp. 1082–1104, 2000.
- [15] P. Bauer and F. S. Marzano, "Numerical simulation and aircraft measurements of melting layer effects on microwave emission and scattering of stratiform precipitation," in *Proc. PIERS'98*, Nantes, France, July 1998, p. 127.
- [16] A. P. Khain and I. Sednev, "Simulation of precipitation formation in the Eastern Mediterranean coastal zone using a spectral microphysics cloud ensemble model," *J. Atmos. Res.*, vol. 43, pp. 77–110, 1996.
- [17] A. P. Khain, I. Sednev, and V. Khvorostyanov, "Simulation of coastal circulation in the eastern Mediterranean using spectral microphysics cloud ensemble mode," *J. Climate*, vol. 9, pp. 3298–3316, 1996.
- [18] S. E. Yuter, R. A. Houze Jr., B. F. Smull, F. D. Marks, Jr., J. R. Daugherty, and S. R. Brodzik, "TOGA-COARE aircraft mission summary images: an electronic atlas," *Bull. Amer. Meteorol. Soc.*, vol. 76, pp. 319–328, 1995.
- [19] J. Turk, F. S. Marzano, and A. Mugnai, "Effects of degraded sensor resolution upon passive microwave precipitation retrievals of tropical rainfall," *J. Atmos. Sci.*, vol. 55, pp. 1689–1705, 1998.
- [20] F. S. Marzano, A. Mugnai, G. Panegrossi, N. Pierdicca, E. A. Smith, and J. Turk, "Bayesian estimation of precipitating cloud parameters from combined measurements of spaceborne microwave radiometer and radar," *IEEE Trans. Geosci. Remote Sensing*, vol. 37, pp. 596–613, Jan. 1999.
- [21] C. Kummerow, W. Barnes, T. Kozu, J. Shiue, and J. Simpson, "The Tropical Rainfall Measuring Mission (TRMM) sensor package," *J. Atmos. Ocean. Tech.*, vol. 15, pp. 809–817, 1998.
- [22] S. K. Mitra, O. Vohl, M. Ahr, and H. R. Pruppacher, "A wind tunnel and theoretical study of the melting behavior of atmospheric ice particle. IV: Experiment and theory for snow flakes," *J. Atmos. Sci.*, vol. 47, 1990.
- [23] S. A. Rutledge and P. V. Hobbs, "The mesoscale and microscale structure and organization of clouds and precipitation in mid-latitudes cyclones. VIII: A model for the 'seeder-feeder' process in warm frontal rain bands," *J. Atmos. Sci.*, vol. 40, pp. 1185–1206, 1983.
- [24] C. G. Bohren and L. J. Battan, "Radar backscattering of microwaves by spongy ice spheres," *J. Atmos. Sci.*, vol. 39, pp. 2623–2628, 1982.
- [25] P. Chylek, V. Srivastava, R. G. Pinnick, and R. T. Wang, "Scattering of electromagnetic waves by composite spherical particles: Experiment and effective medium approximations," *Appl. Opt.*, vol. 27, pp. 2936–2404, 1988.
- [26] R. Meneghini and L. Liao, "Comparisons of cross sections for melting hydrometeors as derived from dielectric mixing formulas and a numerical method," *J. Appl. Meteorol.*, vol. 35, pp. 1658–1670, 1996.
- [27] R. Meneghini and L. Liao, "Effective dielectric constants of mixed-phase hydrometeors," *J. Atmos. Ocean. Tech.*, vol. 17, 2000.
- [28] P. Bauer, L. Schanz, and L. Roberti, "Correction of three-dimensional effects for passive microwave remote sensing of convective clouds," *J. Appl. Meteorol.*, vol. 37, pp. 1619–1632, 1998.
- [29] H. J. Liebe, P. Rosenkranz, and G. A. Hufford, "Atmospheric 60 GHz oxygen spectrum: New laboratory measurements and line parameters," *J. Quant. Spec. Rad. Trans.*, vol. 48, pp. 629–643, 1992.
- [30] F. S. Marzano, A. Mugnai, E. A. Smith, X. Xiang, J. Turk, and J. Vivekanandan, "Active and passive remote sensing of precipitating storms during CaPE. Part II: Intercomparison of precipitation retrievals from AMPR radiometer and CP-2 radar," *Meteorol. Atmos. Phys.*, vol. 10, pp. 29–54, 1994.
- [31] N. Pierdicca, F. S. Marzano, G. d'Auria, P. Basili, P. Ciotti, and A. Mugnai, "Precipitation retrieval from spaceborne microwave radiometers using maximum a posteriori probability estimation," *IEEE Trans. Geosci. Remote Sensing*, vol. 34, pp. 831–846, July 1996.
- [32] C. D. Kummerow, W. S. Olson, and L. Giglio, "A simplified scheme for obtaining precipitation and vertical hydrometeor profiles from passive microwave sensors," *IEEE Trans. Geosci. Remote Sensing*, vol. 34, pp. 12313–1232, Sept. 1996.
- [33] W. S. Olson, C. D. Kummerow, G. M. Heymsfield, and L. Giglio, "A method for combined passive-active microwave retrievals of cloud and precipitation parameters," *J. Appl. Meteorol.*, vol. 35, pp. 1763–1789, 1996.
- [34] G. d'Auria, F. S. Marzano, N. Pierdicca, P. Basili, and P. Ciotti, "Rain retrieval for passive microwave observations: A comparison and a choice," in *Proc. IGARSS'95*, Firenze, Italy, July 10–14, 1995, pp. 1136–1137.
- [35] G. d'Auria, F. S. Marzano, N. Pierdicca, R. Pinna Nossai, P. Basili, and P. Ciotti, "Remotely sensing cloud properties from microwave radiometric observations by using a modeled cloud data base," *Radio Sci.*, vol. 33, pp. 369–392, 1998.
- [36] T. Iguchi and R. Meneghini, "Intercomparison of single-frequency methods for retrieving a vertical rain profile from an airborne or spaceborne radar data," *J. Atmos. Ocean. Technol.*, vol. 11, pp. 1507–1516, 1994.
- [37] Z. S. Haddad, S. L. Durden, and E. Im, "Stochastic filtering of rain profiles using radar, surface-referenced radar, or combined radar-radiometer measurements," *J. Appl. Meteorol.*, vol. 35, pp. 229–242, 1996.
- [38] Y. C. Hong, C. D. Kummerow, and W. S. Olson, "Separation of convective and stratiform precipitation using microwave brightness temperature," *J. Appl. Meteorol.*, vol. 38, pp. 1195–1213, 1999.
- [39] F. S. Marzano, J. Turk, P. Ciotti, S. Di Michele, and N. Pierdicca, "Potential of combined spaceborne microwave and infrared radiometry for near real-time rainfall attenuation monitoring along earth-satellite links," *Int. J. Satellite Commun.*, to be published.

**Frank Silvio Marzano** (S'89–M'99) received the laurea degree (cum laude) in electrical engineering and the Ph.D. degree in applied electromagnetics from the University "La Sapienza," Rome, Italy, in 1988 and 1993, respectively.

In 1993, he collaborated with the Institute of Atmospheric Physics, CNR, Rome, Italy. From 1994 to 1996, he was with the Italian Space Agency, Rome, Italy, as a Postdoctoral Researcher. After being a Lecturer with the University of Perugia, Perugia, Italy, in 1997, he joined the Department of Electrical Engineering, University of L'Aquila, L'Aquila, Italy, where he presently holds the position of Assistant Professor. His current research concerns passive and active remote sensing of the atmosphere from ground-based, airborne, and spaceborne platforms, with a particular focus on precipitation using microwave and infrared data, development of inversion methods, radiative transfer modeling of scattering media, and scintillation and rain-fading analysis along satellite microwave links.

Dr. Marzano received the Young Scientist Award of the XXIV General Assembly of the International Union of Radio Science (URSI) in 1993. In 1998, he was the Recipient of the Alan Berman Publication Award (ARPAD) from the Naval Research Laboratory, Washington, DC.

**Peter Bauer** received the degree in meteorology from the University of Cologne, Cologne, Germany, in 1989 and the Ph.D. from the University of Hamburg, Hamburg, Germany, in 1992.

Since 1989, he has been with the German Aerospace Center, German Remote Sensing Data Center, Koeln, Germany. He was a Postdoctoral Researcher with NOAA/NESDIS, from 1993 to 1994, and received two Guest Scientist appointments with NASA Goddard Space Flight Center, Greenbelt, MD, and CETP-IPSL. His research interests focus on all aspects of microwave retrievals of hydrometeors.